



NATIONAL ENERGY TECHNOLOGY LABORATORY



Natural Gas Hydrate Research

Award Number: Hydrates 2013.07.02

Project Period: October 1, 2013 – September 30, 2014

Quarterly Progress Report

Fiscal Year 2014, Quarter 3

April 1, 2014 – June 30, 2014

Yongkoo Seol, Technical Coordinator

Prepared by
U.S. Department of Energy
National Energy Technology Laboratory
Office of Research and Development

Prepared for
U.S. Department of Energy
National Energy Technology Laboratory
Strategic Center for Natural Gas and Oil



List of Authors

Yongkoo Seol, ORD Technical Coordinator

Gary Sames, ORD Project Coordinator

George Guthrie, ORD Focus Area Lead

Jeffery Ilconich, RES Activity Manager

Table of Contents

1.0	Executive Summary	1
2.0	Goals and Objectives.....	2
3.0	Technical Highlights, Results, and Discussion	3
	Task 1.0 Project Management and Outreach	3
	Task 2.0 Reservoir Simulation of Gas Hydrates Production Field Tests	4
	Subtask 2.1 Simulations of Long-Term Production Scenarios: Depressurization and CO ₂ Exchange.....	4
	Subtask 2.2 International Code Comparison Problem Set Based on Ignik Sikumi	11
	Task 3.0 Developing Constitutive Models of Various Hydrate-Bearing Sands.....	15
	Subtask 3.1 Laboratory Measurements of Geomechanical Strength and Deformability	17
	Subtask 3.2 Developing Constitutive Models of Various Hydrate-Bearing Sands.....	22
	Task 4.0 Assessment of Gas Exchange Processes of CH ₄ Hydrate with CO ₂ under Reservoir Conditions	25
	Subtask 4.1 Gas Exchange Mechanism with Raman Spectroscopy	26
	Subtask 4.2 Gas Exchange Kinetics Measurements in the Presence of Free Water	26
	Subtask 4.3 Data Exchange and Comparative Analysis of Gas Exchange Rates at Various Conditions	28
	Task 5.0 Pore Scale Visualization and Characterization of Hydrate-Bearing Sediments.....	28
	Subtask 5.1 Pore Scale Visualization of Hydrate-Bearing Sediments with High Resolution X-Ray CT Scanners	29
	Subtask 5.2 Grain Scale Constitutive Modeling for Hydrate-Bearing Sediments	30
4.0	Risk Analysis	35
5.0	Milestone Status	35
6.0	Schedule Status	38
7.0	Budget and Cost Status	38
8.0	References.....	39

List of Appendices

Appendix A: Budget and Cost Status	A-1
--	-----

List of Figures

Figure 1: V_{shale} and Hydrate Saturation Correlation for the Ignik Sikumi #1 Well.....	5
Figure 2: L-Pad Area and Cross Section.....	5
Figure 3: Well 1 Gas Rate Profile.....	6
Figure 4: Hydrate Distribution after 1, 2, 3, and 4 Years of Production from Well-1.....	7
Figure 5: Temperature and Pressure Distribution after 0 and 5 Years of Production from Well-1.	7
Figure 6: 3D Grid Structure of Mount Elbert Site.	8
Figure 7: Hydrate Saturation Distribution at the Mount Elbert Site.	9
Figure 8: Sectional View of Initial Hydrate Distribution.....	9
Figure 9: Sectional View of Hydrate Distribution after 2 Months, 4 Months, and 2 Years of Depressurization.	10
Figure 10: Areal View of (a) Initial Hydrate Distribution and (b) after 2 Years of Depressurization.	10
Figure 11: 3D Fault-Bound Gas Production Rate Profile.	11
Figure 12: Reservoir Domain Used for CO ₂ Injection Simulations.....	12
Figure 13: Reservoir Domain Used for CO ₂ Injection Simulations.....	13
Figure 14: Pressure Distribution in the Domain.	14
Figure 15: Temperature Distribution in the Domain.....	14
Figure 16: Hydrate Saturation in the Domain.	14
Figure 17: Gas Saturation in the Domain.....	14
Figure 18: Aqueous Saturation in the Domain.....	15
Figure 19: Peak Deviator Stress versus Hydrate Saturation at Various Effective Confining Stresses (Comparison between NETL and Other Group Data).	19
Figure 20: Peak Deviator Stress versus Effective Confining Stress at Various Hydrate Saturations (Comparison between NETL and Yun et al., Data).	19
Figure 21: Normalized Peak Deviator Stress Versus Hydrate Saturation.....	20
Figure 22: Secant Elastic Modulus Versus Hydrate Saturation at Various Effective Confining Stresses (Comparison between NETL and Other Group Data).	21
Figure 23: Secant Elastic Modulus versus Effective Confining Stress at Various Hydrate Saturations (Comparison between NETL and Yun et al., Data).	21
Figure 24: Normalized Secant Elastic Modulus Versus Hydrate Saturation.	22

Figure 25: Undrained Triaxial Tests from C Code, No Hydrates Case. 23

Figure 26: Undrained Triaxial Tests from FLAC3D, No Hydrates Case. 23

Figure 27: Undrained Triaxial Tests from C Code, $S_H=26\%$ 24

Figure 28: Undrained Triaxial Tests from FLAC3D, $S_H=26\%$ 24

Figure 29: Modeling of Dissociation in the Middle of a Triaxial Test. 25

Figure 30: The Composition of CH_4 Collected from Outlet Gas Stream in CO_2 (l)- CH_4 exchange..... 27

Figure 31: The Composition of CH_4 Collected from Outlet Gas Stream and CH_4 Recovery Rate Calculated from Accumulative Gas Amount Collected in Backpressure Syringe Pump in $[CO_2+N_2]$ - CH_4 exchange. 28

Figure 32: Reconstruction CT Images Using Paganin’s Single Distance Algorithm. (a) Conventional Reconstructed CT Images Have Sharp Gray Value Jumps at Boundaries of Different Phases. (b) By Using the Paganin’s Single Distance Algorithm to Reconstruct CT Images, the Phase-Contrast Artefacts Can Be Removed. 29

Figure 33: High-Pressure Beryllium Chamber on the Micro-CT Station. 30

Figure 34: Hydrate Effect on Fluid Flow Tortuosity in Hydrate-Bearing Sediments. (a) Fluid Fluxed (Red Tubes) and the Critical Flow Path (Blue Tubes) across the Pore Network. (b) The Fluid Flow Tortuosity Oscillates with Hydrate Saturation, but the Generation Trend of the Tortuosity Increases with Hydrate Saturation..... 31

Figure 35: Pore Structure Extraction from CT Images. (a) 3D Micro-CT Images of F110 Sands. (b) Extracted Pore Network Structure from the CT Image. The Green Bubbles Represent the Pores and Their Volume is Scaled to the Bubble Size. The Blue Lines Represent the Throat Connecting Neighboring Pores and the Line Thickness Reflects the Pore Throat Size. 32

Figure 36: In Unconsolidated Sandy Specimen, the Pore Connectivity (cn) Increases with Pore Volume or Pore Radius. 33

Figure 37: Natural Gas Hydrate Research Cost Performance Histogram (\$ x 1,000). 38

List of Tables

Table 1: Reservoir Rock Parameters Used 12

Table 2: Relative Permeability and Capillary Pressure Function Parameters..... 13

Table 3: Experimental Information of Tri-Axial Compression Test on Non-Cementing HBS 17

Table 4: Natural Gas Hydrate Research Support Milestone Status 36

Table 5: Natural Gas Hydrate Research Field Work Proposal Budget Status (Current Period)..... A-2

Table 6: Natural Gas Hydrate Research Field Work Proposal Budget Status (Cumulative)..... A-3

Acronym List

Acronym	Descriptive Name
AK-DNR	Alaskan Department of Natural Resources
ANS	Alaska North Slope
CMU	Carnegie Mellon University
CO ₂	Carbon Dioxide
CT	Computed Tomography
RHOB	Density
DOE	Department of Energy
DT	Sonic
FAL	Focus Area Lead
FEHM	Finite Element/Finite Volume Heat and Mass Transfer Computer Code
FPM	Federal Project Manager
FWP	Field Work Proposal
GR	Gamma Ray
GUI	Graphical User Interface
HBS	Hydrate-Bearing Sediment
HQ	Headquarters
HRS	HydrateResSim
NETL	National Energy Technology Laboratory
NMR	Nuclear Magnetic Resonance
ORD	Office of Research and Development
PBU	Prudhoe Bay Unit
Pitt	University of Pittsburgh
PMP	Project Management Plan
PSU or Penn State	The Pennsylvania State University
R&D	Research and Development
Res	Resistivity
RES	Research and Engineering Services
RUA	Regional University Alliance
SARS	Safety Analysis and Review System
SCNGO	Strategic Center for Natural Gas and Oil
S _H	Hydrate Saturation
SHC	Shale Content
SOPO	Statement of Project Objectives
S _w	Water Saturation

Acronym	Descriptive Name
TC	Technical Coordinator
THM	Thermal-hydrological-geomechanical
TM	Technology Manager
TMo	Technical Monitor
TVDSS	Total Vertical Depth
URS	URS Corporation
USGS	United States Geological Survey
VSHC	Volume of Shale Content
WVU	West Virginia University

1.0 Executive Summary

The National Energy Technology Laboratory (NETL) Office of Research and Development (ORD) supports the U.S. Department of Energy (DOE) National Gas Hydrate Research and Development (R&D) Program by providing numerical predictions on gas production activities and experimental estimations of physico-chemical reaction characteristics including geomechanical strength, gas exchange kinetics, and hydrate accumulation patterns in pore space. ORD's research will include combined efforts from the NETL-Regional University Alliance (RUA), Oak Ridge Alliance Universities – Oak Ridge Institute of Science and Education (ORAU-ORISE), URS Corporation (URS), and URS subcontractors.

Continuing efforts on numerical simulations in Subtask 2.1 include history matching for the Iğnik Sikumi field test for the gas hydrate exchange trial using Mix3HydrateResSim. A series of reservoir simulations were performed to model the long-term response to depressurization. Laboratory experiments continued, particularly in the area of geomechanical reference tests to correct the rubber sleeve effect on mechanical strength measurements with hydrate-bearing sediments, and CO₂-CH₄ gas exchange kinetics with continuous flowing column setup. The two reference mechanical tests with rubber rods were used to derive the effect of a rubber sleeve, which were incorporated into the actual test. Maximum deviator stress increased with hydrate saturation when the saturation was higher than 30 percent, and elastic modulus showed the same pattern. An SMP subloading critical state constitutive model was developed and verified using the available data from the literature. Application of the model to the NETL test data is also in progress. Pore scale characterization of hydrate-bearing sediments using a micro CT scanner has been performed using analogue materials and pore network models have also been developed based on the 3D micro CT images.

This quarterly progress report provides the list of tasks, status of the work, major accomplishments, and updates regarding milestone dates. Research highlights this quarter include:

- Geostatistical representations of the PBU-based system incorporating extensive well-log correlations and a 3D representation of the fault-bounded Mount Elbert system have been generated to more extensive and computationally expensive simulation results.
- A series of code comparison problems including a CO₂ injection scenario in a 2D reservoir system filled with CH₄ hydrate was developed for distribution to the code comparison group.
- Our multi-stage tri-axial test results from a non-cementing hydrate-bearing sediment (HBS), particularly peak deviator stress (q_{peak}) and secant elastic modulus (E_{50}), were analyzed in comparison with similar single-stage tri-axial test results by [1] Ebinuma et al., 2005; [2], [3] Masui et al., 2005, 2008; [4] Yun et al., 2007. The analysis reveals that the effect of previous overloading imposed by multi-stage test method on q_{peak} can be minimal, whereas that on E_{50} cannot be negligible. E_{50} can increase by previous overloading history.
- An acoustic test on a CH₄-HBS sample during hydrate dissociation by depressurization was completed and its results are currently being analyzed.
- The geomechanical/acoustic tests on CO₂-HBS were started and are currently in progress.
- The CH₄ production efficiency from CH₄ hydrate bearing sand with free water is low in column mode. In particular, [CO₂+N₂]-CH₄ exchange shows the CH₄ recovery rate less than 7%.

- High resolution Raman spectrometer was set-up for examining gas exchange mechanism, providing detailed spectra for various molecular bondings, which would help to identify the free water release during exchange.
- The Paganin's single distance algorithm was implemented to suppress phase-contrast artefacts and improve phase separation. This will be beneficial to identify the hydrate phase from the water phase in computed tomography (CT) images, which has long been a challenge as the densities of these two phases are very close. Also, the CT system and peripheral components are ready to synthesize hydrate-bearing sediments in the beryllium vessel.
- A 2D pore network model was developed and employed to investigate hydrate effects on fluid flow tortuosity and water permeability in HBS. This work was accepted for publication in Geophysical Research Letters. The 3D pore network structure was extracted from CT images of F110 sands with fundamental grain/pore characteristics computation and flow process simulation pending advancement in FY14-Q4.

2.0 Goals and Objectives

The National Gas Hydrate Research and Development (R&D) Program has worked to accelerate the determination and realization of gas hydrate's resource potential and to better understand the role of gas hydrate in the environment. This Gas Hydrates Research project has been developed with a diverse set of research activities, performed by the U.S. DOE, NETL-ORD, and the RUA, to fill multiple needs within the National Gas Hydrate R&D program. The objective of the research project is to obtain pertinent, high-quality information on gas hydrates that will benefit the development of models and methods for predicting the behavior of gas hydrates in their natural environment under natural conditions and production scenarios. NETL-ORD supports major gas hydrate production field tests by providing numerical predictions on fluid migration, gas production, and potential reactions occurring during gas production activities; as well as, by providing fundamental understanding and knowledge on hydrate behavior derived from experimental investigations on thermal, hydrological, geomechanical, and reactive responses of hydrate. The proposed research consists of numerical modeling efforts, including:

- Simulations of long-term production tests and international code comparison studies for Iñnik Sikumi test.
- Laboratory experimental tests on geomechanical measurements.
- Gas exchange kinetics and mechanism tests.
- High resolution visualizations of hydrate distributions in porous media.
- General assistance and participation on domestic and international gas hydrate research and development activities.

3.0 Technical Highlights, Results, and Discussion

The current progress of the work completed in FY14-Q3 is provided below. For each task and subtask, a detailed description is provided for the accomplishments this period, changes in approach, problems or delays, changes in key personnel, and technology transfer activities and products produced.

Task 1.0 Project Management and Outreach

This project is technically managed by the ORD Focus Area Lead (FAL). The FAL provides overall technical direction and guidance to the NETL-RUA research tasks. This project is implemented by a Technical Coordinator (TC) who provides the day-to-day technical and administrative management of the Field Work Proposal (FWP) tasks. Problems that arise during the execution of the various tasks will first be addressed by the TC, and if necessary the problem will be elevated to the attention of the FAL for resolution. If the support of the Strategic Center for Natural Gas and Oil (SCNGO) is needed to resolve any research issue, the FAL will do so during periodic meetings with the SCNGO Technology Manager (TM). Issues of a more administrative and reporting nature will be resolved with the FWP Technical Monitor (TMO).

Accomplishments this Period:

The project management activity produces internal and public reports required to demonstrate competent technical and administrative execution of the project. Deliverables submitted and accomplishments met during this activity period are as follows:

- The FY14-Q2 report was submitted to SCNGO on April 30, 2014.
- The production of an updated FWP is underway. The FY15 FWP and PMP will be submitted to SCNGO in July 2014.
- Regular monthly task and subtask level group meetings were conducted among DOE, URS, and NETL-RUA personnel.
- Monthly invoice reviews were conducted prior to the ORD approval of the invoices.
- Milestone and deliverable status were monitored and updated.

Changes in Approach:

Nothing to report during this activity period.

Problems or Delays:

Nothing to report during this activity period.

Changes in Key Personnel and Partnerships:

Nothing to report during this activity period.

Technology Transfer Activities or Product Produced:

Nothing to report during this activity period.

Task 2.0 Reservoir Simulation of Gas Hydrates Production Field Tests

Objectives

- Provide modeling predictions utilizing current capabilities for past and future potential field tests, including a long-term depressurization test on the ANS and the ConocoPhillips CO₂-CH₄ exchange test. Modeling results will be compared with available field data.
- Coordinate an international effort for the analysis of the Igñik Sikumi CO₂-CH₄ exchange test and cross-validation of the participating reservoir simulation codes using test data sets and data from the Igñik Sikumi test.

Scope of Work

Simulations of field tests in the ANS are designed to test the efficacy of using depressurization and CO₂ injection as a means to initiate gas production from Arctic hydrate deposits below the permafrost. The short-term goal of this task is to provide modeling predictions for future potential field tests (e.g., long-term depressurization test) and to analyze and extrapolate longer-term responses from recent field tests (e.g., ConocoPhillips CO₂-CH₄ exchange test).

Accomplishments this Period:

Subtask 2.1 Simulations of Long-Term Production Scenarios: Depressurization and CO₂ Exchange

A number of simulation scenarios have been constructed and performed on both L-Pad-like and Mount Elbert-like hydrate-bearing systems. For the L-Pad area, available well logs have been correlated, in which hydrate saturation from resistivity or nuclear magnetic resonance (NMR) data are available with V_{shale} from gamma ray logs available in 75 wells. These correlations cover a large extent of the Prudhoe Bay Unit (PBU) L-Pad hydrate deposit. Additionally, the 3D system at the Mount Elbert site was constructed and will be simulated for varying depths and temperatures representing various sites in the Alaskan Department of Natural Resources (AK-DNR) deferred tracts.

Dipping structure, fault-bounded up dip (similar to PBU L-Pad)

A sample correlation for the Igñik Sikumi #1 well is shown in Figure 1.

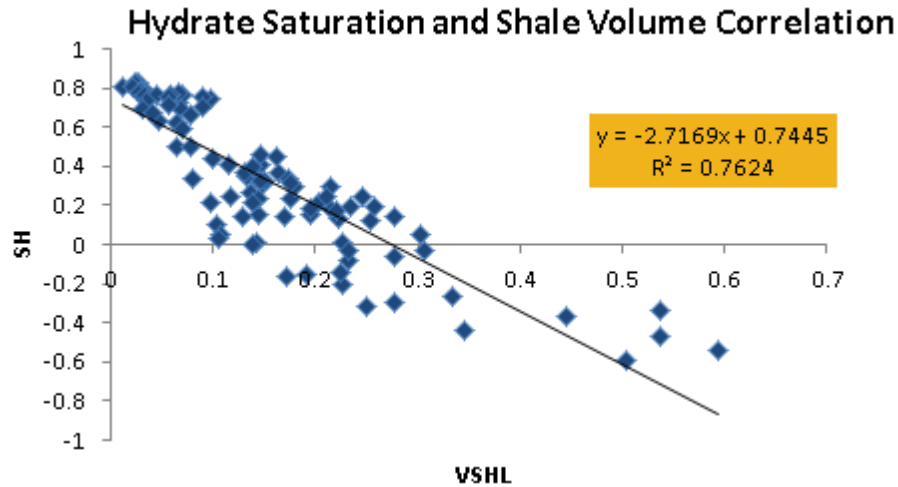


Figure 1: V_{shale} and Hydrate Saturation Correlation for the Ignik Sikumi #1 Well.

Creating geostatistical realizations of the L-Pad deposit began and preliminary simulations were completed.

A 3D representation of the L-Pad area and cross section near a new well site, Well 1, is shown in Figure 2.

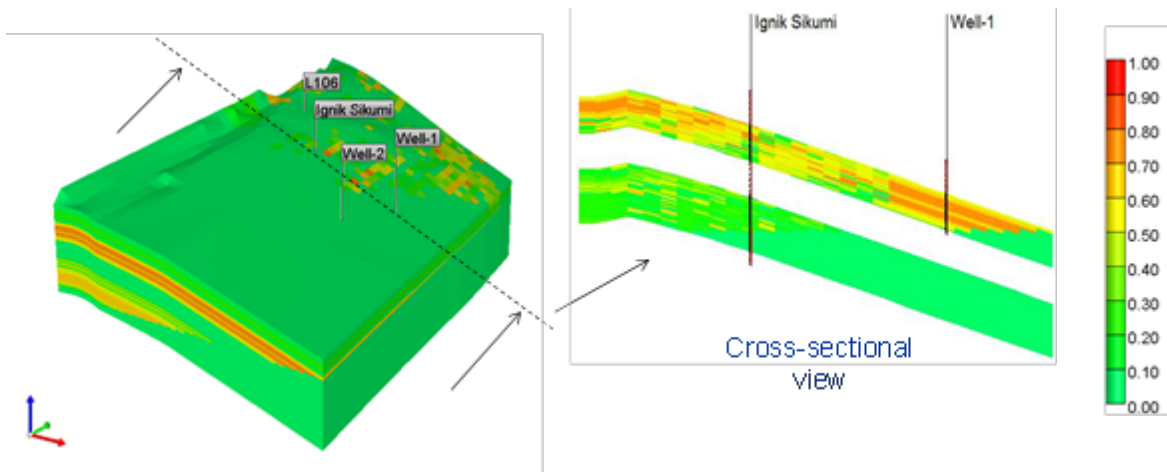


Figure 2: L-Pad Area and Cross Section.

The model, shown in Figure 2, is an extracted sub model from a parent model and was built using contour data from a 5 ft. interval, provided by the United States Geological Survey (USGS). The model is bounded in the west by a system of vertical faults, which almost form a three-way closure and in the east by the hydrate-water contact at 685 m (2,248 ft.). The northern and southern boundaries were chosen as guided by the fault system in the west boundary.

The sub model grid measures 950 x 1800 x 45 m and is divided into 30 x 50 x 80 simulation grid blocks in the x, y, and z directions, respectively.

Due to the complexity of the hydrate dissociation process, grid refinements were performed in the region of high hydrate saturations and also in regions near the well bore. The effective radius of the well bore grid was 0.6 m (smallest possible, to guarantee simulation convergence for this system) and the thickness of the high hydrate saturation layers was 0.43 m, while other layers had a thickness of 0.87 m.

Figure 3 shows the gas production rate profile for one geostatistical realization around Well 1. The production rate increases almost linearly with time. The maximum gas production rate achieved at the end of the fifth year is around 15,000 m³/day, which is higher than the previous case where the maximum production rate of 12,000 m³/day was achieved at the end of the fifth year.

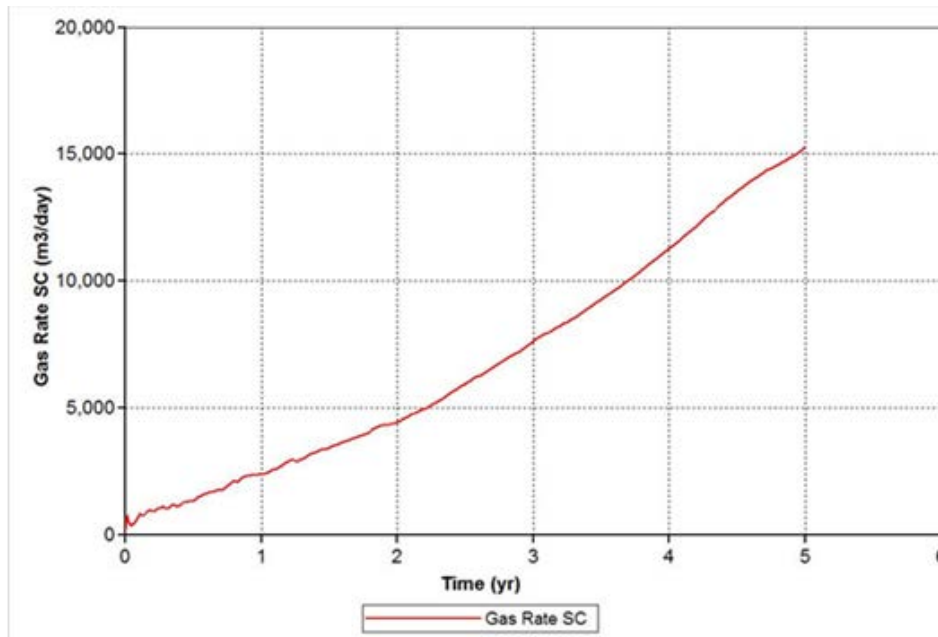


Figure 3: Well 1 Gas Rate Profile.

The distribution of hydrate saturation along the x - z plane is shown in Figure 4. It can be seen from Figure 4 that much lower hydrate saturation is present in C2 layer as compared to C1 layer which is obtained by the geostatistical realization. As the time progresses hydrate gets dissociated and the region around the wellbore of Well 1 gets depleted in hydrate saturation. Figure 5 shows pressure and temperature profile at 0 and 5 years of hydrate production.

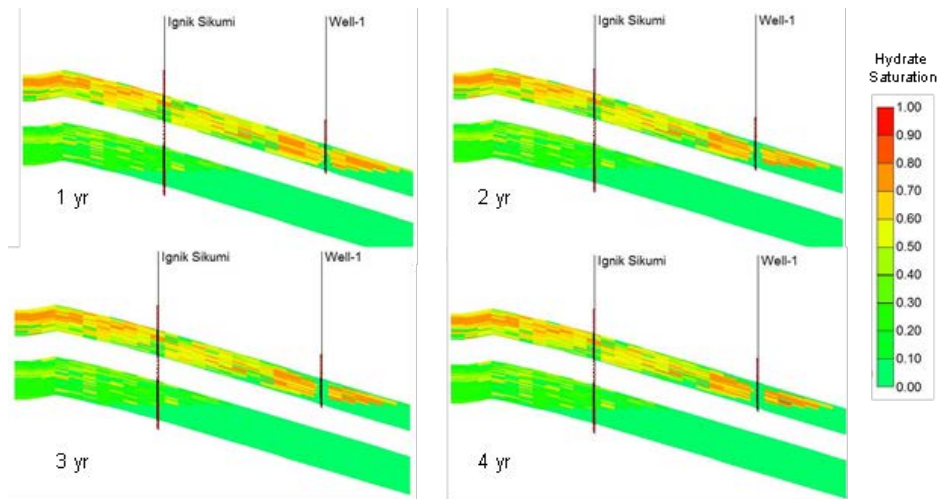


Figure 4: Hydrate Distribution after 1, 2, 3, and 4 Years of Production from Well-1.

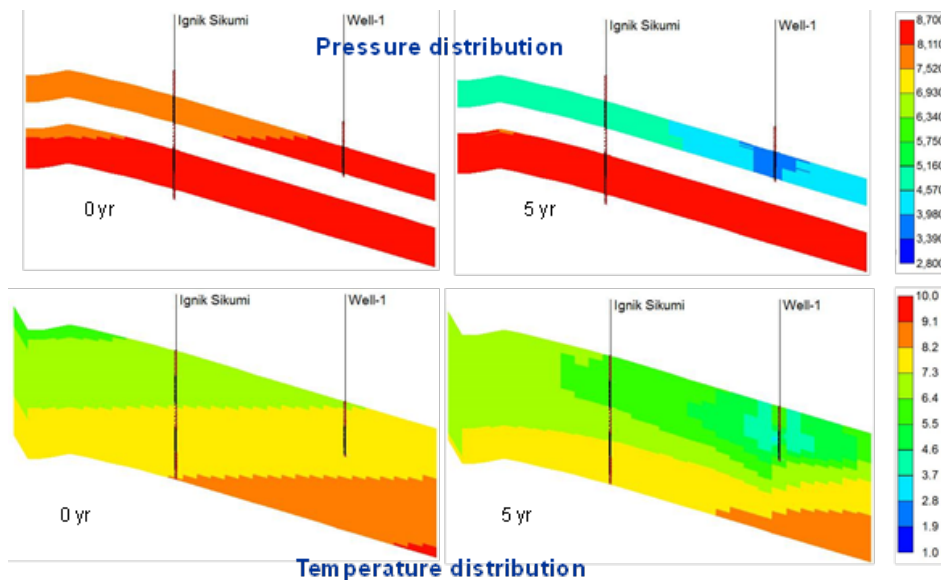


Figure 5: Temperature and Pressure Distribution after 0 and 5 Years of Production from Well-1.

Fault-block structure for Site 2 evaluation (similar to Mount Elbert)

A 3D model of Mount Elbert is being developed as an improvement on the existing 2D model. The goal is to adapt this model for the deeper and warmer Site 2 model.

USGS xyz data of depths to the top of the C sand were used to create the reservoir model structure shown in Figure 6.

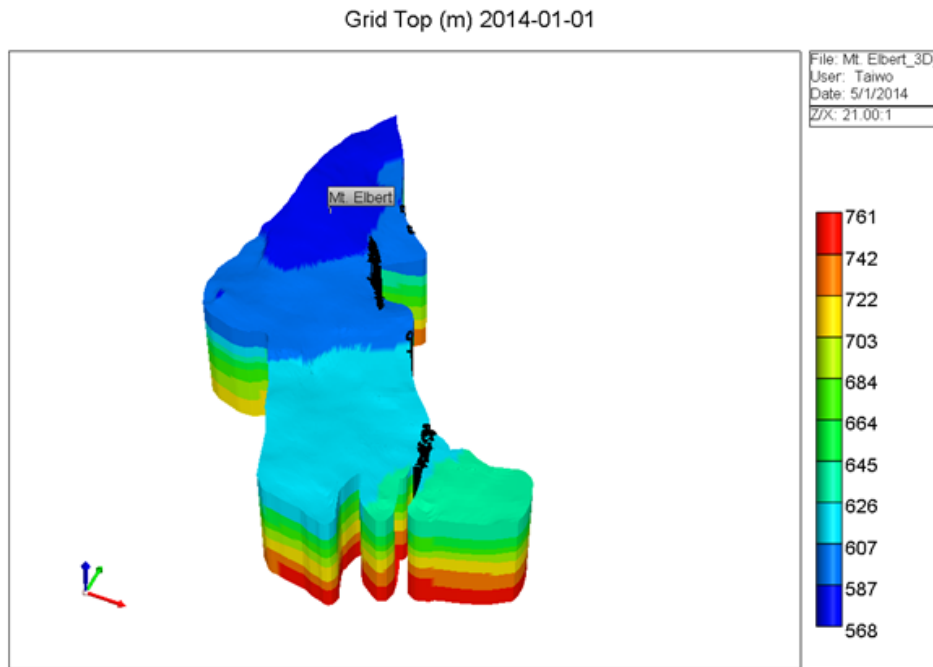


Figure 6: 3D Grid Structure of Mount Elbert Site.

The model has an overall grid thickness of 70 m, with overburden and underburden shale of thickness 10 m each. Each layer in the hydrate-bearing sand is 0.25 m thick.

To estimate the hydrate distribution in the reservoir volume, the following steps were taken:

- The available surface (x-y) hydrate distribution was pinned to the 29th layer, which is the layer with the highest hydrate saturation value, per the Mount Elbert well log-inferred vertical S_H profile (Figure 7).
- The vertical S_H profile, interpreted from the Mount Elbert well log, was normalized by dividing each of the S_H values in each layer by that of the layer with the highest S_H value.

This normalized profile was then used as a multiplication factor by which the original surface hydrate saturation distribution was multiplied to give an estimate of the surface hydrate saturation distribution in each layer.

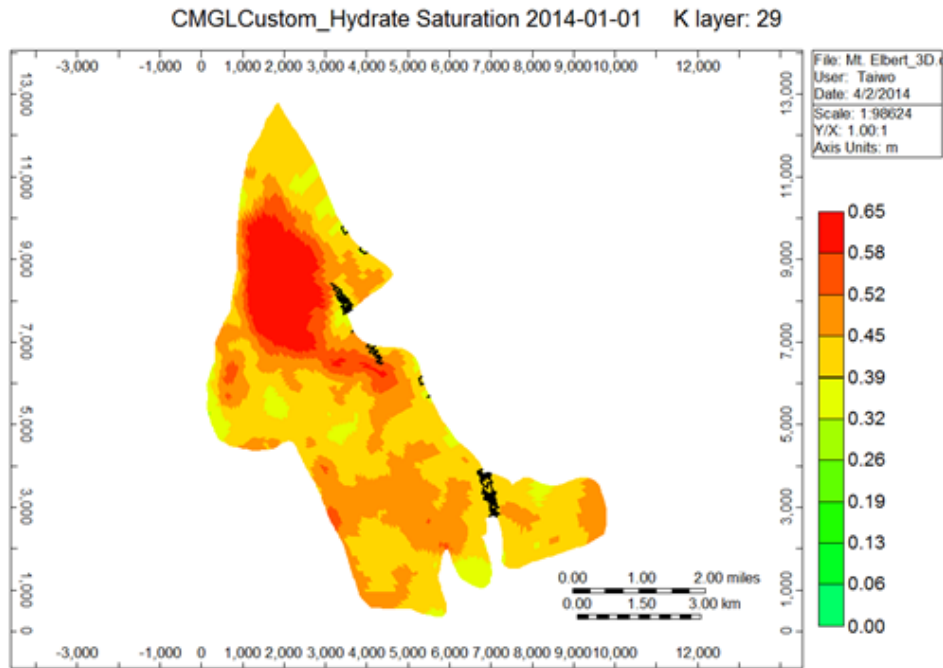


Figure 7: Hydrate Saturation Distribution at the Mount Elbert Site.

The bounding faults were modeled by setting the permeability of the fault blocks to zero. All other initial reservoir conditions and well constraints were the same as the 2D Mount Elbert problem.

Simulations are currently being run to investigate the performance of this model for the first five years of production. Figure 8 shows a sectional view of the initial hydrate distribution in the Mount Elbert site 3D simulation and Figure 9 and Figure 10 show hydrate distribution after 2 months, 4 months, and 2 years of depressurization. Figure 11 shows cumulative gas production rates over the simulation period.

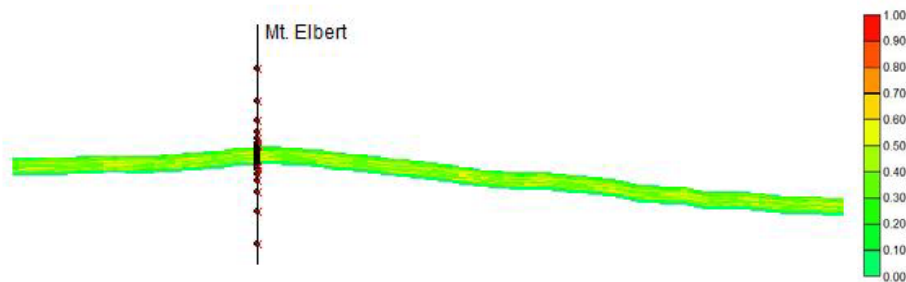


Figure 8: Sectional View of Initial Hydrate Distribution.

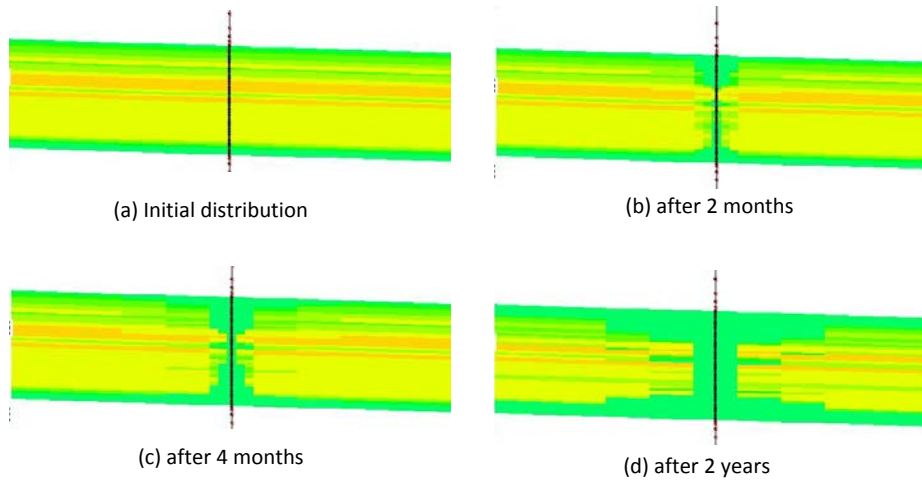


Figure 9: Sectional View of Hydrate Distribution after 2 Months, 4 Months, and 2 Years of Depressurization.

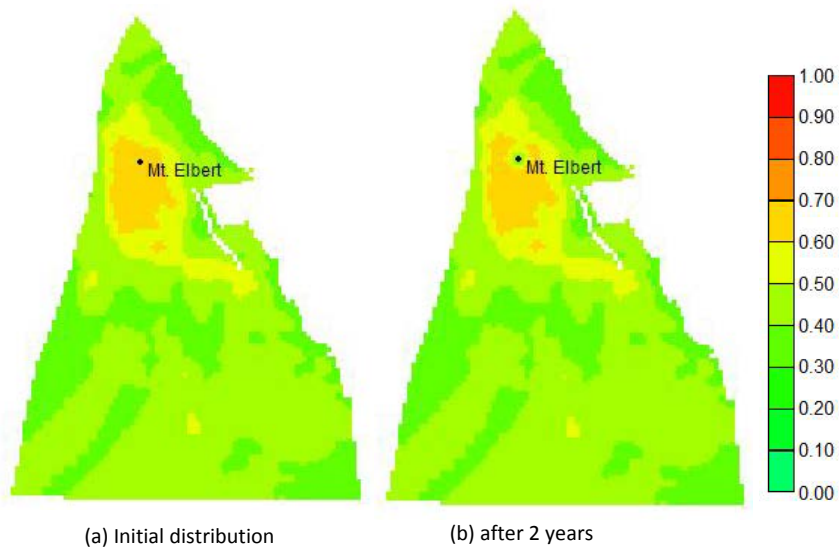


Figure 10: Areal View of (a) Initial Hydrate Distribution and (b) after 2 Years of Depressurization.

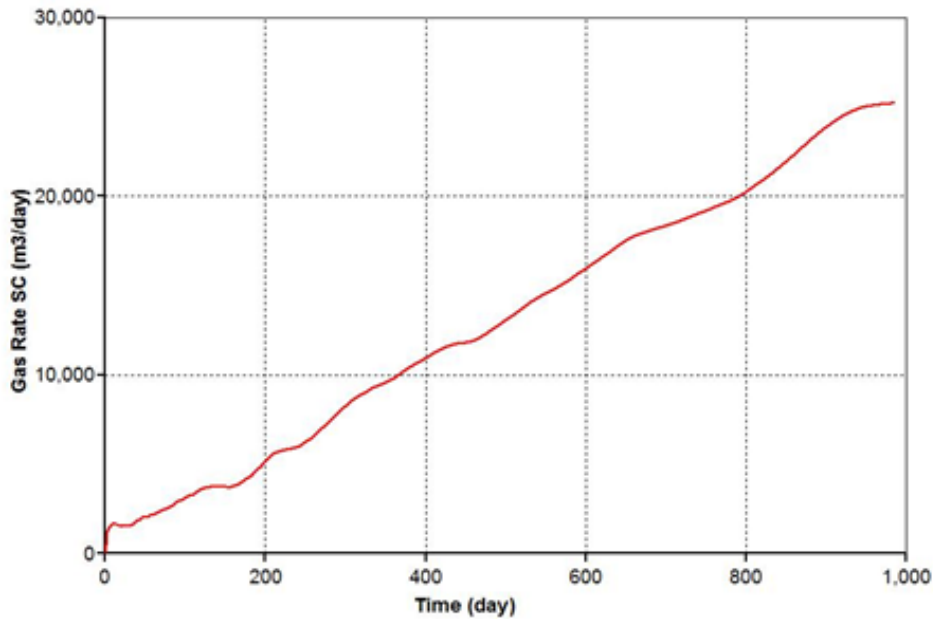


Figure 11: 3D Fault-Bound Gas Production Rate Profile.

Summary

In FY14-Q2, simulation results were reported using homogeneous model descriptions for the PBU L-Pad deposits and for a radial representation of the Mount Elbert-like model. This quarter, producing geostatistical representations of the PBU-based system that incorporate extensive well-log correlations and a 3D representation of the fault-bounded Mount Elbert system were the focus. These simulations are much more extensive and computationally expensive than the previous quarter's results.

Subtask 2.2 International Code Comparison Problem Set Based on Iğnik Sikumi

A series of code comparison problems were developed and simulated.

Additionally, a CO₂ injection scenario in a 2D reservoir system filled with CH₄ hydrate for distribution to the code comparison group was developed and simulated.

CO₂ Injection into a CH₄ hydrate reservoir domain:

The reservoir domain is shown in Figure 12.

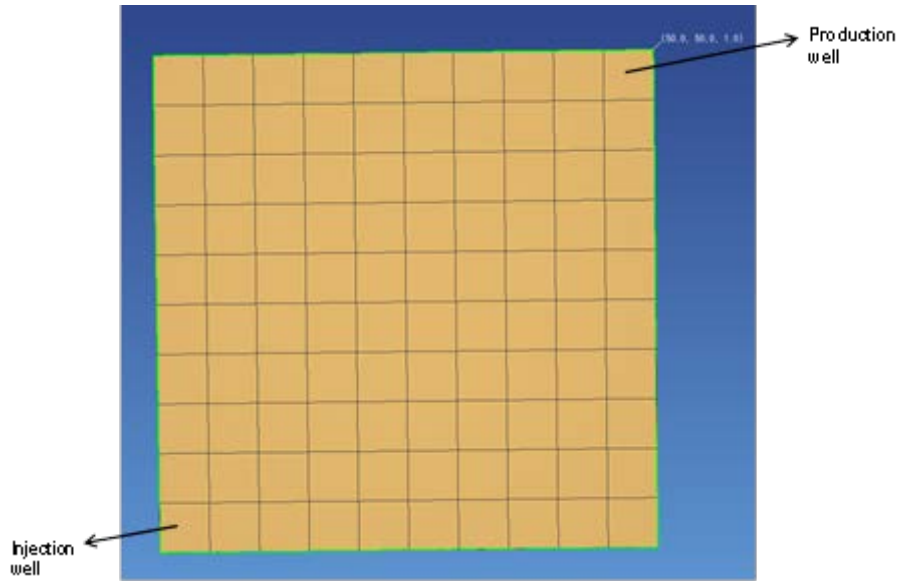


Figure 12: Reservoir Domain Used for CO₂ Injection Simulations

A 10×10 Cartesian domain is used with the size of each volume element equal to 5m (shown in Figure 12). An injection well is considered at left side lower corner (0, 0) of the reservoir and the production well is considered at the right side upper corner (50, 50). Hence, the distance between the two wells is nearly 70m.

Initial Conditions:

The initial conditions include 30% hydrate saturation at excess gas saturation (i.e., free CH₄ excess conditions) and aqueous saturation of the domain is assigned to be very low. The temperature of the domain is maintained at 1.5°C.

During the production simulations, pure gaseous CO₂ was injected (at 3.9 MPa, 4°C) into the domain, the production well was modeled as constant pressure boundary surfaces, which is maintained at 3 MPa. Other relevant rock parameters and hydrological properties used for simulation are listed in Tables 1 and 2.

Table 1: Reservoir Rock Parameters Used

Parameters	Value Used
Porosity	0.3
Density	2650 kg/m ³
Thermal Conductivity	2.0 W/m K
Specific heat	750 J/kg K
Pore Compressibility	5.0×10 ⁻¹⁰ Pa ⁻¹

Table 2: Relative Permeability and Capillary Pressure Function Parameters

Relative Permeability	Aziz and Stone Equation
S_{irA}	0.15
S_{irG}	0.05
n	3
Capillary Pressure	Van Genuchten Function
S_{irA}	0.14
n	1.84
α	10

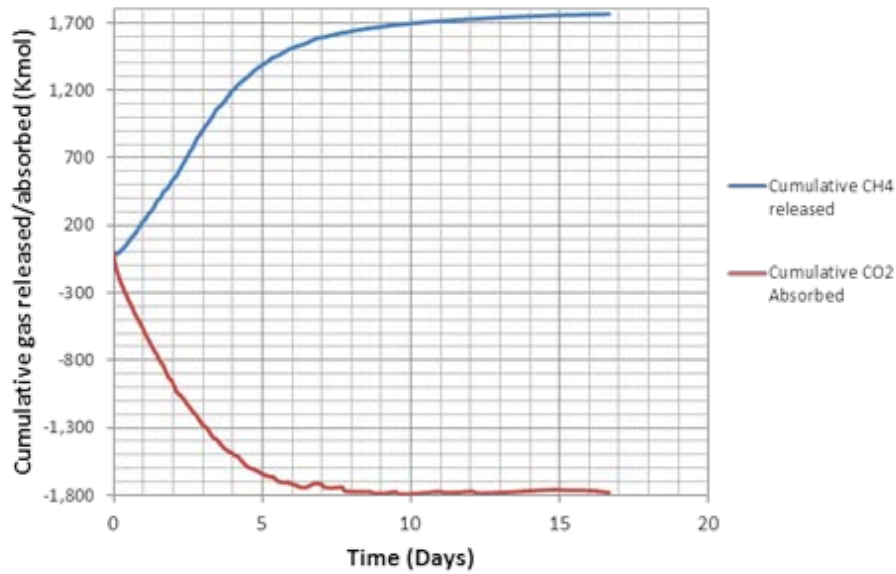


Figure 13: Reservoir Domain Used for CO₂ Injection Simulations.

The amounts of gases released/absorbed from the hydrate in the domain are shown in Figure 13, for an injection pressure of 3.9 MPa. The negative numbers suggest that the gas is absorbed, forming hydrate while the positive profile implies that gas is released. Therefore, from the above figure it is evident that CO₂ is absorbed for hydrate formation, while CH₄ is released from hydrate.

During the initial days of injection, it was observed that CO₂ molecules are used for hydrate formation without CH₄ gas release from hydrate. It can also be observed that the total number of moles of CO₂ absorbed for hydrate formation is more than the total number of CH₄ gas moles released, which implies that the CO₂ forms hydrate with the available free water.

In the previous case, the total number of CO₂ moles is not greater than the total moles of CH₄, unlike this case. The main reason for this observation is that previously excess gas saturation is considered.

The following figures (Figures 14-18) are the system conditions at the end of 15-day simulation time.

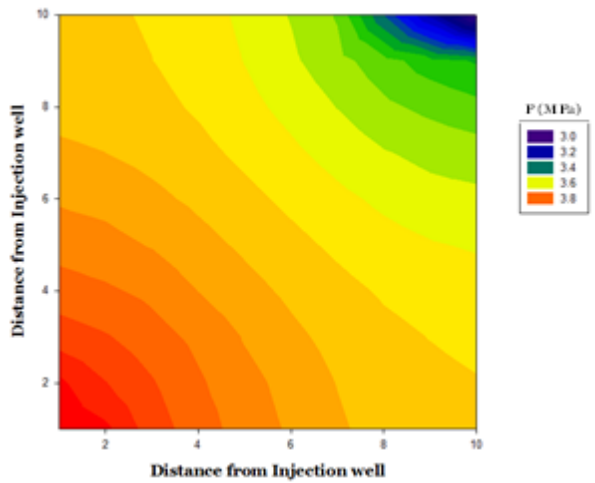


Figure 14: Pressure Distribution in the Domain.

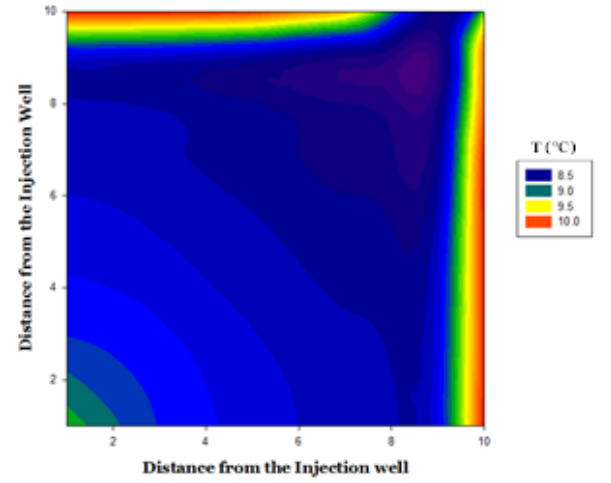


Figure 15: Temperature Distribution in the Domain.

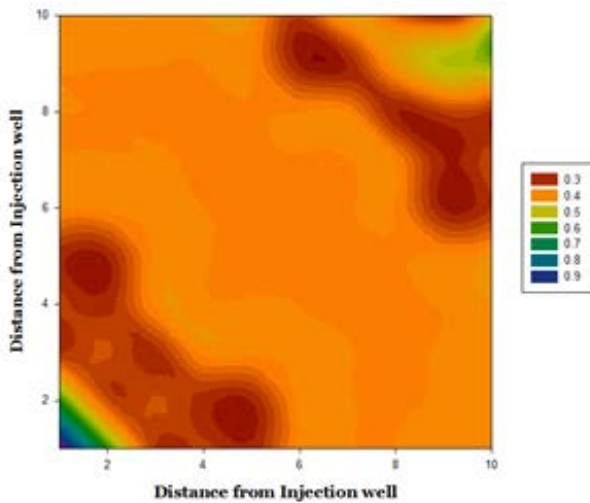


Figure 16: Hydrate Saturation in the Domain.

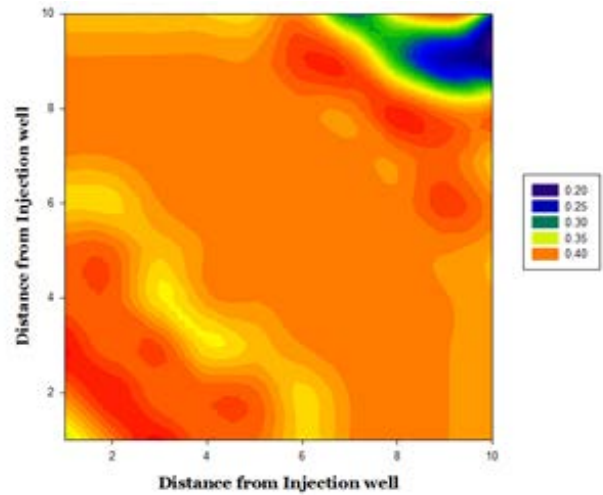


Figure 17: Gas Saturation in the Domain.

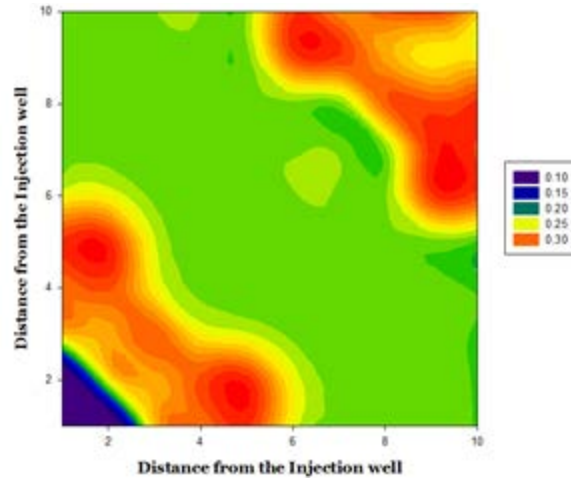


Figure 18: Aqueous Saturation in the Domain.

Changes in Approach:

For Subtask 2.1, we have taken a contingency approach to simulation sites. The exact location of a potential long-term depressurization test site is yet to be determined, and thus we have proceeded with simulations of the Prudhoe Bay L-Pad hydrate-bearing sands. These simulations are quickly adaptable to other test sites as identified.

Problems or Delays:

The delayed selection of a long-term depressurization test and collection of relevant dataset resulted in a delay in task progress.

Changes in Key Personnel and Partnerships:

Nothing to report during this activity period.

Technology Transfer Activities or Product Produced:

Nothing to report during this activity period.

Task 3.0 Developing Constitutive Models of Various Hydrate-Bearing Sands

Objectives

This task will fulfill two objectives:

1. Develop constitutive models for various hydrate-bearing sediments under in situ overburden pressure and temperature conditions.
2. Provide a rational basis for modeling and predicting the geomechanical behavior and stability of hydrate-bearing sands in the field during gas production (using depressurization and gas exchange). The results of this task will aid in understanding the behavior of hydrate-bearing sediments under gas production and will provide insight that will assist in optimizing the design of future production operations.

Scope of Work

This work will implement and test the constitutive laws of the hydrate-bearing sands developed in FY13 based on the NETL laboratory tests. The constitutive law will be utilized to predict the geomechanical behavior of hydrate-bearing sediments under gas production (dissociation or gas exchange). Additional laboratory tests will be performed to measure mechanical parameters of the sediments with various conditions, such as binary hydrate mixtures during the gas exchange process. The constitutive law will be implemented into a geomechanical analysis code, and this code will work with a multiphase flow code.

Accomplishments this Period:

Subtask 3.1 Laboratory Measurements of Geomechanical Strength and Deformability

The results of the geomechanical test on the non-cementing CH₄-HBS samples, particularly peak deviator stress (q_{peak}) and secant elastic modulus (E_{50}), have been analyzed in comparison with those by other research groups. Table 3 shows basic information of test samples and the method utilized by each group. As shown in Table 3, NETL is the only group to utilize a multi-stage test (MST) method; therefore, the comparison of our data with other teams' data will assist in assessing the effect of loading history imposed by the MST method on the test results.

Table 3: Experimental Information of Tri-Axial Compression Test on Non-Cementing HBS

	NETL	Masui et al., 2005	Ebinuma et al. 2005	Masui et al., 2008	Yun et al., 2007
Sediment Type	Silica sand (F110) + 5% Kaolinite clay	Silica sand (Toyoura)	Silica sand	Natural sandy sediment (Nankai Trough)	Silica sand (F110)
Mean Grain Size, D_{50} (mm)	120 (sand) 1.0 (clay)	180	220	84 ~ 180	120
Porosity, ϕ	0.35 ~ 0.38	0.42 ~ 0.43	0.39 ~ 0.40	0.44 ~ 0.51	0.37 ~ 0.39
Guest Molecule	CH ₄	CH ₄	CH ₄	CH ₄	Tetrahydrofuran (THF)
Hydrate Habit	Non-cementing	Non-cementing	Non-cementing	Non-cementing (?)	Non-cementing
Tri-Axial Test Type	Multi-stage tri-axial	Single-stage tri-axial	Single-stage tri-axial	Single-stage tri-axial	Single-stage tri-axial
Eff. Confining Stress, σ'_o (MPa)	0.69, 1.38, 2.76	1	3	1	0.03, 0.5, 1

Figure 19 shows that q_{max} data from our test and others' tests are located orderly with respect to the applied effective confining stresses (σ'_o); i.e., q_{max} increases with σ'_o . Also, it is observed that the q_{max} increases with the hydrate saturation (S_h) in general, but no significant increase in q_{max} occurs below the hydrate saturation (S_h) of ~30%, which is considered the point where the hydrate formation habit changes from pore-filling to load-bearing.

Our q_{max} data are also compared with those by [4] Yun et al., 2007, which were obtained at various effective confining stresses (σ'_o) with a single-stage test (SST) method (Figure 20). Both cases show that q_{max} increases linearly with increasing σ'_o . The linear increase of q_{max} observed for the MST method indicates that the residual plastic strain imposed on the sample after the previous stages of σ'_o (1st and 2nd stages) can barely influence the q_{max} at second and third stages. This lack of influence on the q_{max} can possibly be explained by considering frictional effect on the failure of unconsolidated sediment during the shearing. Shear strength, which is calculated by q_{max} , is controlled by the friction on interfaces of sediment particles (including soil and/or hydrate particles), and the slip of these interfaces (i.e., shear failure) occurs when the frictional resistance reaches its limit (i.e., friction coefficient). The friction limit, which is considered a particularly dominant factor for determining the shear strength of non-cementing HBS, would not change much unless the shape, size, and gradation of sample particles change significantly, which is hardly believed to occur during the MST. Furthermore, if the reconsolidation of the sample is adequately conducted after each stage of MST, as done in our test, changes in the friction limit can be minimized. With the similar friction limit, the shear failure can occur at the similar q_{peak} that can be obtained from SST under similar S_h and σ'_o . From the data comparison and intuitive understanding of failure mechanism discussed above, it is anticipated that the q_{peak} obtained by the MST can be comparably used along with those from the SST.

The q_{peak} data for each σ'_o case, shown in Figure 19, are normalized with its q_{peak} value at $S_h = 0\%$ ($q_{peak,o}$) (Figure 21). This normalization allows for evaluation of the effect of S_h on q_{peak} at each σ'_o . Figure 21 shows that there is no particular trend of variation in normalized q_{peak} over σ'_o , indicating that the effect of S_h on q_{peak} may not be influenced by σ'_o . This allows a single trend line to be drawn on the normalized q_{peak} data over varying σ'_o and S_h . The trend equation, shown in Figure 21, could be utilized to predict the q_{peak} values for various S_h within the current S_h range of 0 to ~70%, if the $q_{peak,o}$ under a specific σ'_o is known and the σ'_o is within the range of 0.69 to 3MPa. It is also generalized with the normalized data that there is no significant effect of S_h on q_{peak} below $S_h = \sim 30\%$.

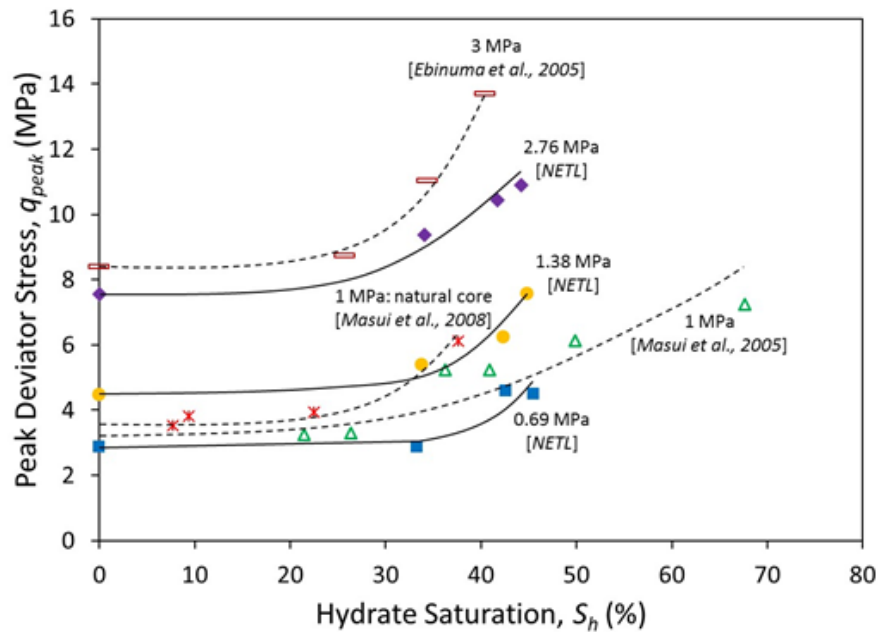


Figure 19: Peak Deviator Stress versus Hydrate Saturation at Various Effective Confining Stresses (Comparison between NETL and Other Group Data).

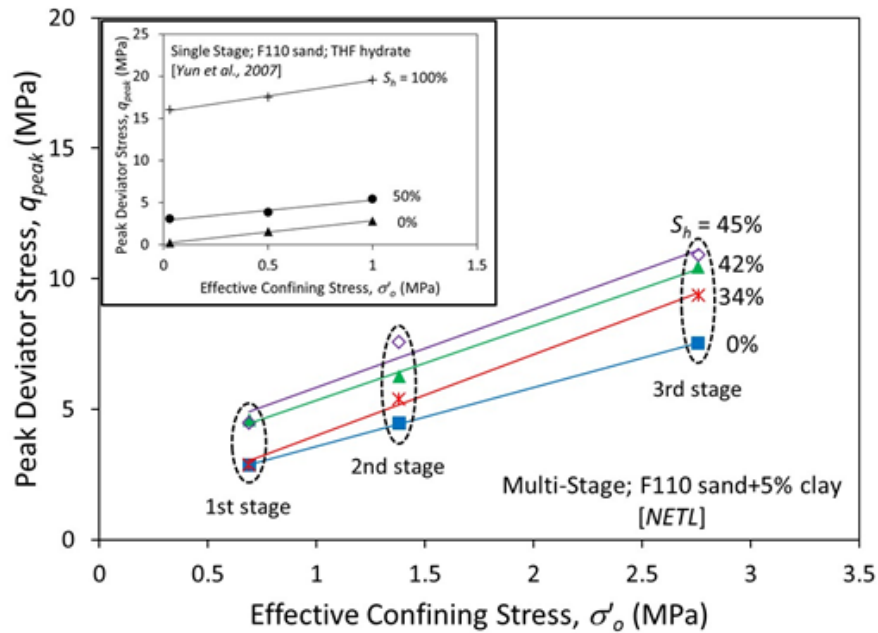


Figure 20: Peak Deviator Stress versus Effective Confining Stress at Various Hydrate Saturations (Comparison between NETL and Yun et al., Data).

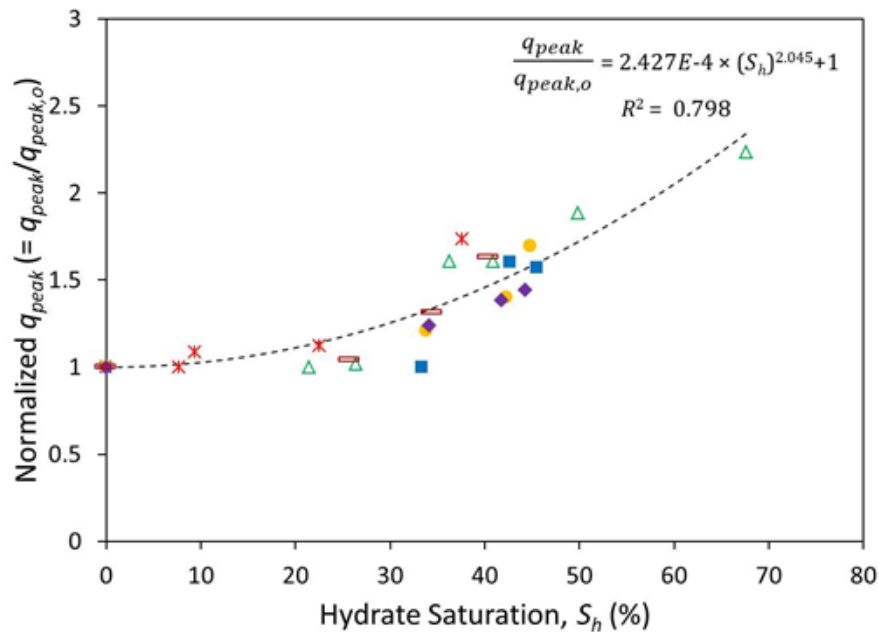


Figure 21: Normalized Peak Deviator Stress Versus Hydrate Saturation.

Figure 22 shows that the secant elastic moduli, E_{50} ($= q_{50}/\epsilon_{a,50}$, where $q_{50} = 50\%$ of q_{peak} and $\epsilon_{a,50} =$ axial strain at q_{50}) increase with σ'_o . The E_{50} also increases with the S_h , but significant E_{50} increase occurs when the S_h passes by $\sim 30\%$, similar to the case of q_{max} .

- Our E_{50} data are also compared with those by [4] Yun et al., 2007 (Figure 23) over σ'_o in log-log scale. It is generally known that the elastic modulus (E) is proportional to a power function of σ'_o , i.e., $E \propto (\sigma'_o)^\beta$, where α and $\beta =$ empirical parameters, and thereby the relationship between the E and σ'_o can be linear in the log-log scale. However, our data barely show good linear relationships in the log-log scale, which Yun et al. data seem to have. This non-linearity in our data indicate that the loading history (i.e., residual plastic strain) from MST method can influence the E_{50} at later σ'_o stages of the test. The observation also suggests that the stress-strain curve from the MST method will be different from that from the SST methods under similar experimental conditions.
- To observe the effect of S_h on E_{50} at different σ'_o , E_{50} data from each σ'_o are normalized by its E_{50} at $S_h = 0\%$ ($E_{50,o}$) (Figure 24). It seems that the effect reduces when the σ'_o increases. When the σ'_o increases, the overall inter-particulate skeletal stiffness increases as well, and thereby the contribution from soil particles to bulk HBS stiffness becomes more dominant than that from the hydrate.

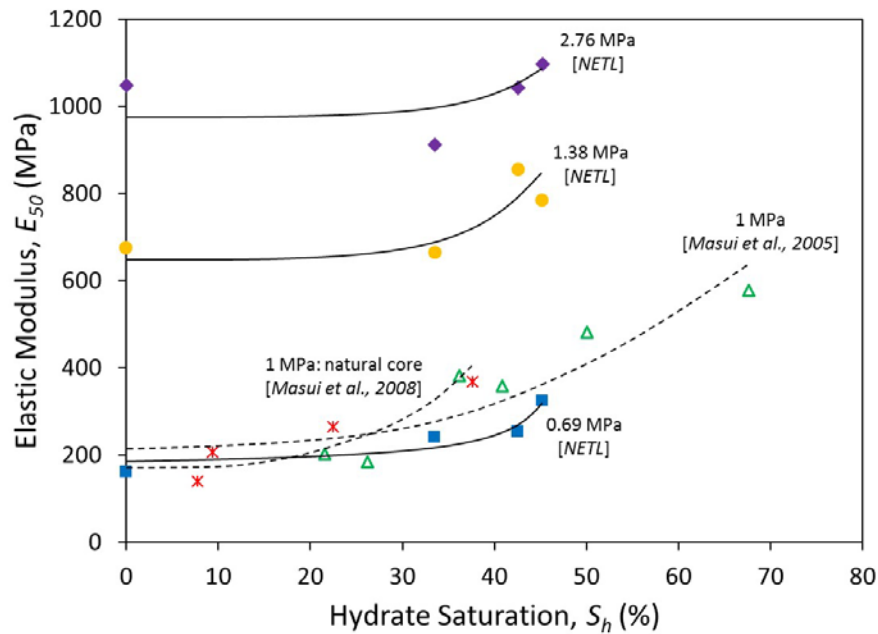


Figure 22: Secant Elastic Modulus Versus Hydrate Saturation at Various Effective Confining Stresses (Comparison between NETL and Other Group Data).

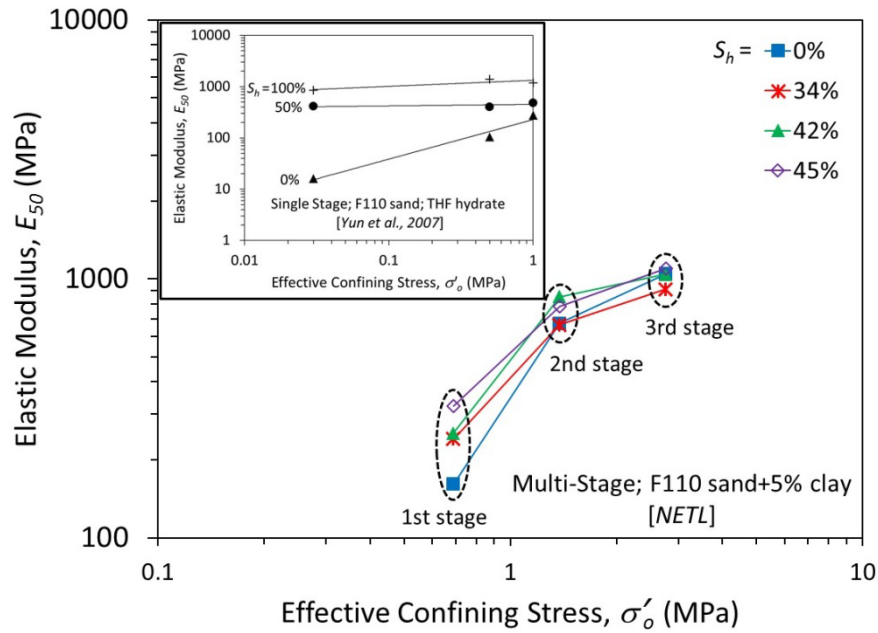


Figure 23: Secant Elastic Modulus versus Effective Confining Stress at Various Hydrate Saturations (Comparison between NETL and Yun et al., Data).

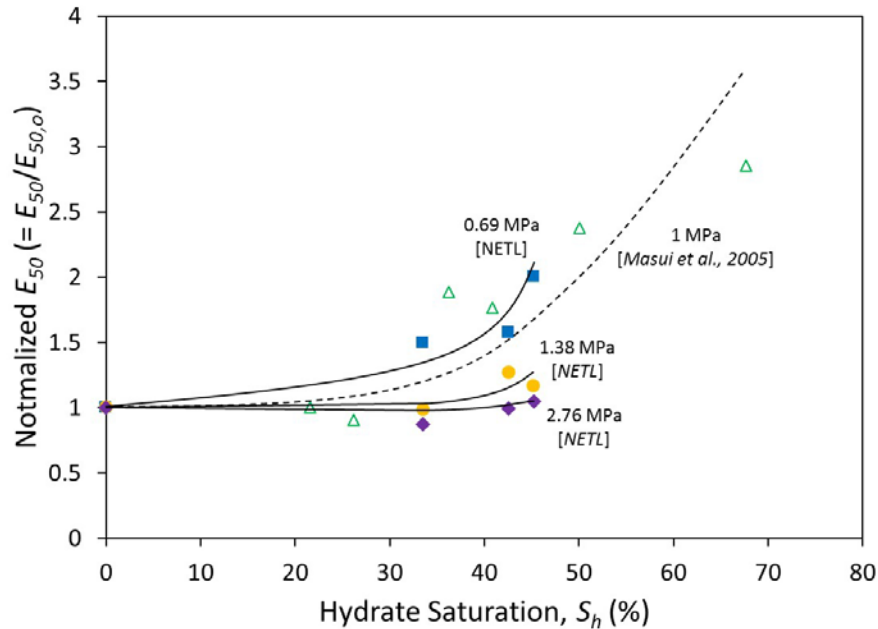


Figure 24: Normalized Secant Elastic Modulus Versus Hydrate Saturation.

References:

- [1] Ebinuma, T., Kamata, Y., Minagawa, H., Ohmura, R., Nagao, J. and Narita, H. (2005), “Mechanical Properties of Sandy Sediment Containing Methane Hydrate,” *Proceedings of the 5th International Conference on Gas Hydrates (ICGH 2005)*, Trondheim, Norway, June 12-16.
- [2] Masui, A; Haneda, H.; Ogata, Y.; and Aoki, K. (2005), “Effects of Methane Hydrate Formation on Shear Strength of Synthetic Methane Hydrate Sediments,” *Proceedings of the 15th International Offshore and Polar Engineering Conference*, Seoul, Korea, June 19-24.
- [3] Masui, A.; Miyazaki, K.; Haneda, H.; Ogata, Y.; Aoki, K. (2008), “Mechanical Characteristics of Natural and Artificial Gas Hydrate-Bearing Sediments,” *Proceedings of the 6th International Conference on Gas Hydrates*, Vancouver, British Columbia, Canada, July 6-10.
- [4] Yun., T. S.; Santamarina, J. C.; and Ruppel, C. (2007), “Mechanical Properties of Sand, Silt, and Clay Containing Tetrahydrofuran Hydrate,” *Journal of Geophysical Research: B-Solid Earth*, Vol. 112, B04106, doi:10.1029/2006 JB 004484.

Subtask 3.2 Developing Constitutive Models of Various Hydrate-Bearing Sands

Implementation in FLAC3D 4.0 has continued. The model for drained tests, undrained tests, and for dissociation effects has been successfully implemented.

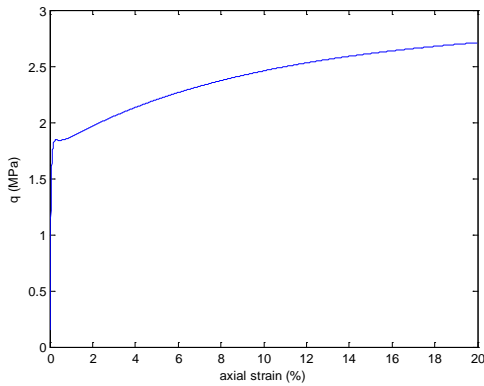
For assessing the undrained test results, two different approaches were adopted. On one hand, C code was used, and we carry out strain controlled undrained tests by:

1. Imposing zero volume strain constraint, namely applying $\epsilon_{vol} = 0$, or $\epsilon_2 = \epsilon_3 = -\epsilon_1 / 2$

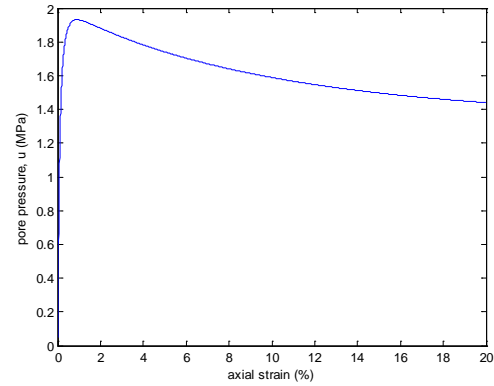
2. Obtaining the pore water pressure from the change in the lateral pressure.

The second approach was to run a coupled analysis in FLAC3D using a fluid bulk modulus of $2 \cdot 10^9$ Pa.

The two approaches gave essentially the same results and thus verified the implementation as seen below. The checks were carried out for both without hydrates and with hydrates (Figures 25-28).

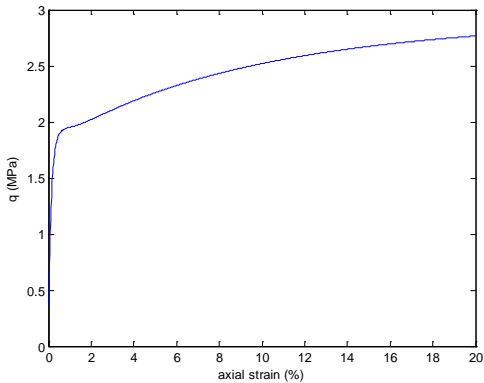


(a) Deviatoric stress, q, versus axial strain

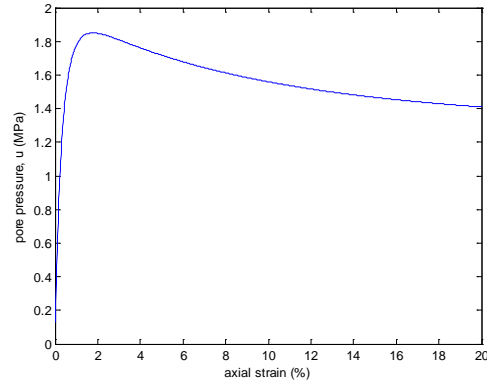


(b) Pore pressure versus axial strain

Figure 25: Undrained Triaxial Tests from C Code, No Hydrates Case.

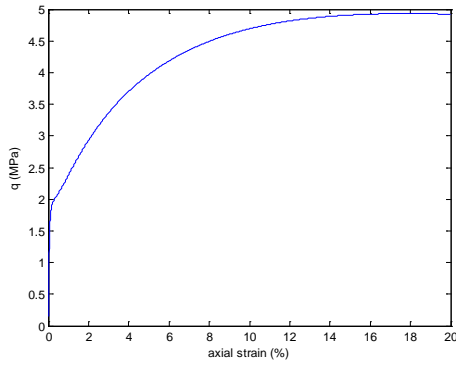


(a) Deviatoric stress, q, versus axial strain

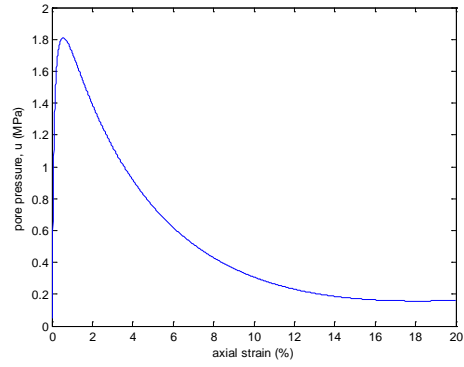


(b) Pore pressure versus axial strain

Figure 26: Undrained Triaxial Tests from FLAC3D, No Hydrates Case.

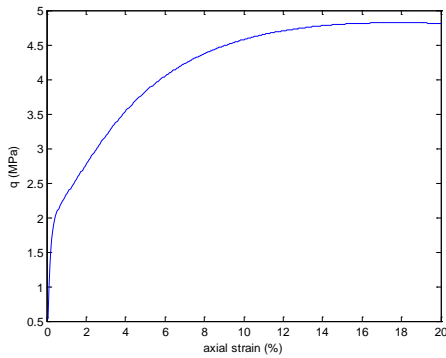


(a) Deviatoric stress, q , versus axial strain

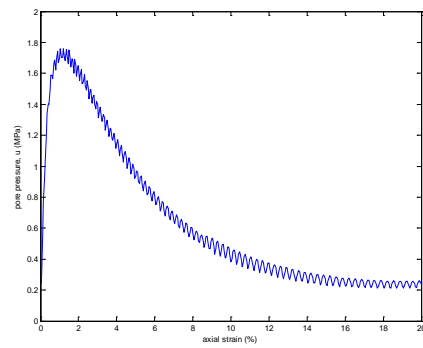


(b) Pore pressure versus axial strain

Figure 27: Undrained Triaxial Tests from C Code, $S_H=26\%$.



(a) Deviatoric stress, q , versus axial strain



(b) Pore pressure versus axial strain

Figure 28: Undrained Triaxial Tests from FLAC3D, $S_H=26\%$.

In our constitutive model, stress could be changed by either imposing a strain, or by introducing a hydrate saturation change as follows,

$$d\sigma' = \frac{[\mathbf{C}^E - \mathbf{C}^E : \frac{\partial f}{\partial \mathbf{t}'} \otimes \frac{\partial f}{\partial \sigma'} : \mathbf{C}^E] : d\epsilon - \mathbf{C}^E : \frac{\partial f}{\partial \mathbf{t}'} \frac{\partial f}{\partial t'_{Ncd}} ab(S_H^G)^{b-1} \chi_1 \chi_2 dS_H}{H + \frac{\partial f}{\partial \sigma'} : \mathbf{C}^E : \frac{\partial f}{\partial \mathbf{t}'}}$$

The first term was introduced in the past, now the second term has been implemented as well. An example of the implementation is given herein. The case models a hydrate-bearing soil with $S_H=30\%$, and after 10% axial strain, the hydrate saturation S_H , was abruptly reduced to 10%. The model shows the stress was sharply relaxed, immediately when dissociation took place, and then it gradually persisted (Figure 29). The sharp drop was modeled by the second term; and the gradual change by the first term of the constitutive model.

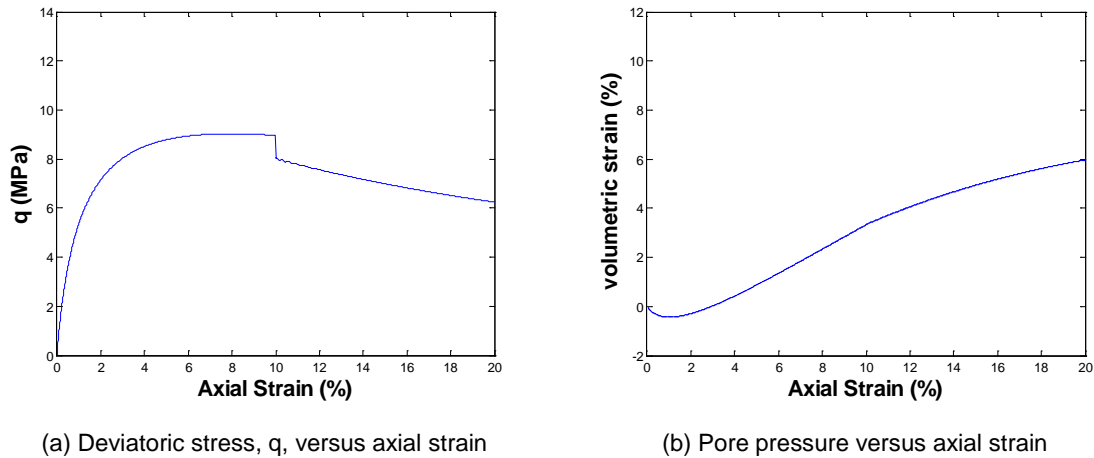


Figure 29: Modeling of Dissociation in the Middle of a Triaxial Test.

Changes in Approach:

Nothing to report during this activity period.

Problems or Delays:

Mechanical tests with the CO₂ hydrate test were delayed due to unexpectedly extended time for brine injection time and sample preparation. The test will be completed by the end of August.

Changes in Key Personnel and Partnerships:

Nothing to report during this activity period.

Technology Transfer Activities or Product Produced:

The paper, entitled “Multi-Properties Characterization Chamber for Hydrate-Bearing Sediments” by Yongkoo Seol, Jeong-Hoon Choi, and Sheng Dai, was submitted to *Review of Scientific Instruments*, and is current being revised for resubmission, according to journal reviewer’s comments.

Task 4.0 Assessment of Gas Exchange Processes of CH₄ Hydrate with CO₂ under Reservoir Conditions

Objectives

- Determine the mechanisms of gas exchange between CO₂ and CH₄ when CO₂ is injected into CH₄-hydrate-bearing sediment for CH₄ production.
- Determine the kinetics of gas exchange in the systems with the presence of free water and varied gas mixtures (CO₂, CH₄, and N₂) within pore space.
- Share/exchange gas exchange kinetics data with LBNL and PNNL for comparative analysis of exchange kinetics data acquired under different reaction conditions.

- Utilize experimental results to enhance understanding of gas exchange processes as a gas production technology and help identify optimum conditions (such as composition of feed gas and pore gas and free water saturation) for sustained CH₄ production.

Scope of Work

The mechanisms of replacement of CH₄ with CO₂, within a system containing CH₄ hydrate, will be experimentally assessed using Raman spectroscopy. Experimental tests will be continued which focus on measuring the replacement kinetics in both the batch and column systems, where CO₂ or CO₂ and N₂ mixed gas will be injected in the presence of free water. It is also planned to share/exchange the resultant gas exchange kinetics data with LBNL and PNNL for comparative analysis.

Accomplishments this Period:

Subtask 4.1 Gas Exchange Mechanism with Raman Spectroscopy

Nothing to report during this activity period.

Subtask 4.2 Gas Exchange Kinetics Measurements in the Presence of Free Water

Liquid CO₂-CH₄ Exchange Kinetics in Batch Mode

1. Procedures

A high pressure tri-axial vessel was used to synthesize CH₄ hydrate in sand samples. Pore and confining pressures were controlled by an ISCO 500D syringe pump (Teledyne Technologies, USA), and temperature was measured by K-type thermocouples (OMEGA, USA), at a spot 0.7 cm deep inside from the fluid-injecting end of the sample.

F110 sands with an average diameter of 120 μm (U.S. Silica) were moistened with de-ionized water for targeted water saturation of 45% in the pore spaces between sand grains before being uniformly packed into the rubber sleeve. The tight compaction of sands into the rubber sleeve (internal volume of 159.1 cm³) yielded a porosity of 37% for the sand sample and water saturation (S_w) of 44% in the pore volume.

CH₄ hydrate was formed by pressurizing the vessel with CH₄ to 1100 psi. After hydrate formation reaction was completed, CH₄ gas was discharged until pressure reached a phase equilibrium pressure of 4.55 MPa at 5.6°C. Free water was introduced by partial dissociation of CH₄ hydrate. The water released from the hydrate phase was calculated on the basis of pressure increase caused by hydrate dissociation. The resulting free water saturated the pore space of 14% in the sand pack.

For [CO₂ + N₂]-CH₄ exchange, CH₄ in the pore space was replaced with CO₂ + N₂ (23:77) mixed gas at 2.7°C where [CO₂ + N₂] was supplied to the vessel in constant flow of 5 ml/min whereas gas in the vessel was discharged in the constant pressure mode of 8.34 MPa. For CO₂ (l)-CH₄ exchange, CO₂ (l) was supplied to replace CH₄ at a constant rate of 5 ml/min under the constant back pressure of 5.7 MPa. When the composition of CH₄ in the reactor was lower than 1%, gas flow rate decreased to 0.06 and 0.033 ml/min for the mixed gas and CO₂ (g) injection systems, respectively, and the gas exchange process in hydrate phase was assumed to start. The gas was collected from the outlet stream and syringe pump side to analyze the composition in the gas phase by using a Shimadzu DS2014 gas chromatograph with a TCD detector and He carrier gas.

2. Results

Figure 30 shows the variation of CH₄ concentration collected from the outlet stream. CH₄ gas was not produced continuously in both CO₂ (l) and [CO₂ + N₂] injection systems. The compositions of CH₄ were in the range of 0 ~ 2.11% and 0 ~ 1.94% for CO₂ (l) and [CO₂ + N₂], respectively. More than half of the total measurements were 0%. The gas composition from the back-pressure syringe pump side was also measured to calculate accumulative amount of CH₄ recovered from CH₄ hydrate phase in [CO₂ + N₂]-CH₄ exchange. The gas was collected when the pump was filled with the fluid. The results demonstrate the CH₄ recovery rate at less than 7% in the presence of free water in the sediments (Figure 31).

Low efficiency, particular in CO₂ (l) injection, is contrary to our previous batch result which reached 52% of recovery rate in the presence of free water. Low efficiency in column mode could be explained for CO₂ (l) injection system by the following:

- High driving force of CO₂ (l) would make the free water readily converted to CO₂ hydrate.
- Formed CO₂ hydrate blocks the pathway to access the CH₄ hydrate for CO₂ molecules.
- Continuously flowing CO₂ (l) would bypass CH₄ hydrate domains blocked by CO₂ hydrate rather than diffuse into or penetrate CO₂ hydrate.

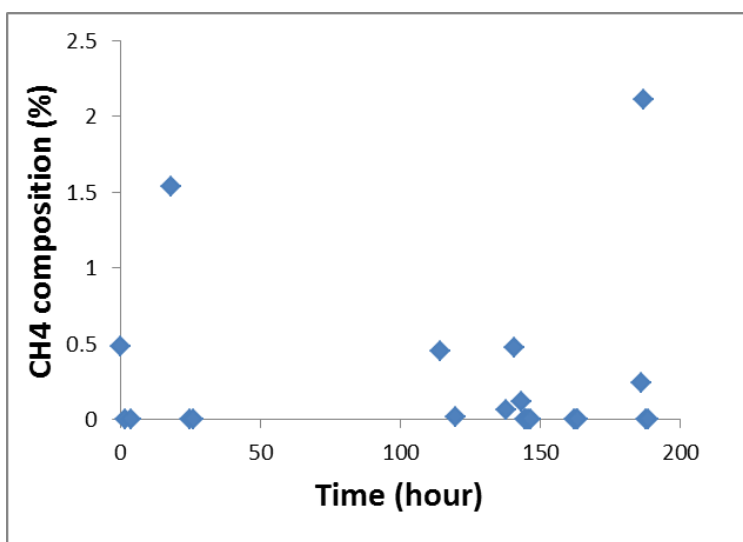


Figure 30: The Composition of CH₄ Collected from Outlet Gas Stream in CO₂ (l)-CH₄ exchange.

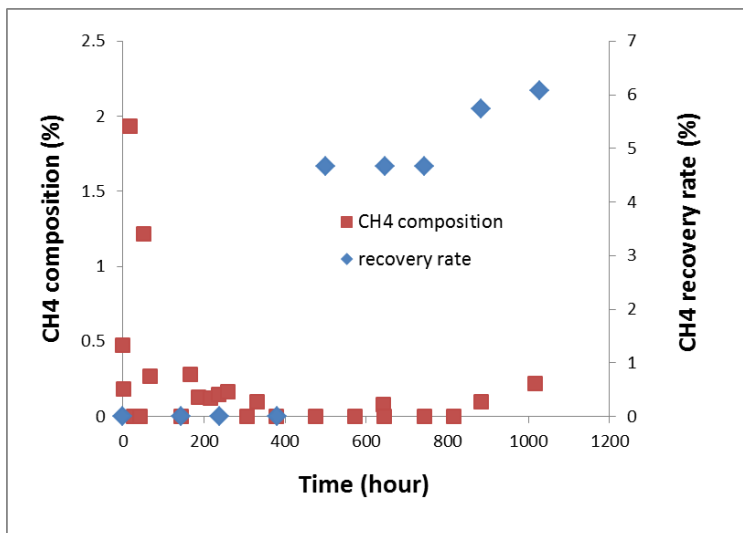


Figure 31: The Composition of CH₄ Collected from Outlet Gas Stream and CH₄ Recovery Rate Calculated from Accumulative Gas Amount Collected in Backpressure Syringe Pump in [CO₂+N₂]-CH₄ exchange.

Subtask 4.3 Data Exchange and Comparative Analysis of Gas Exchange Rates at Various Conditions

Nothing to report during this activity period.

Changes in Approach:

The team is focusing on CO₂ gas injection with higher S_w condition rather than (CO₂+N₂) mixed gas system.

Problems or Delays:

The exchange mechanism is delayed due to a SARS issue on the Raman laser.

Exchange kinetics are delayed because the experimental procedure needs to be modified to avoid undesirable hydrate formation from free water during the gas exchange process.

Changes in Key Personnel and Partnerships:

Nothing to report during this activity period.

Technology Transfer Activities or Product Produced:

Nothing to report during this activity period.

Task 5.0 Pore Scale Visualization and Characterization of Hydrate-Bearing Sediments

Objective

The objective of this task includes: (1) visualizing pore spaces within lab-synthesized hydrate-bearing sediments, of cementing or non-cementing habit, subjected to hydrate productions and gas exchange tests, (2) obtaining high resolution images showing hydrate distribution habits within pore spaces, (3) performing grain-scale modeling of fluid flow using the 3D models developed based on the high resolution CT images, and (4) developing insight into how hydrate accumulation habits in pore space

impacts the potential of gas production by providing sustained hydrate dissociation with thermal stimulations, supporting mechanical integration of pore structures, and providing flow pathways for gas and liquids during production.

Scope of Work

Laboratory formed hydrate-bearing samples will be subjected to high resolution x-ray CT imaging. The NETL high resolution micro-XCT scanner will be used to obtain micron-scale voxel resolution images of hydrate-bearing samples and capture pore scale phenomenon. A pressure-temperature control system built around the CT scanner will be connected to the beryllium pressure vessel, where hydrate samples will be formed for fluid injection, gas exchange, and hydrate aging experiments.

Accomplishments this Period:

Subtask 5.1 Pore Scale Visualization of Hydrate-Bearing Sediments with High Resolution X-Ray CT Scanners

Due to the ring artefact and localized beam hardening of X-rays, obtained CT images always have sharp jumps at boundaries of two different phases (see the gray value profile in Figure 32(a). The Paganin's single distance algorithm ([5] Weitkamp et al., 2011) has been used to reconstruct the raw X-ray projections and obtain CT images with removed artefacts. This technique is beneficial to phase separation during later image processing, such as distinguishing the hydrate phase from the water phase.

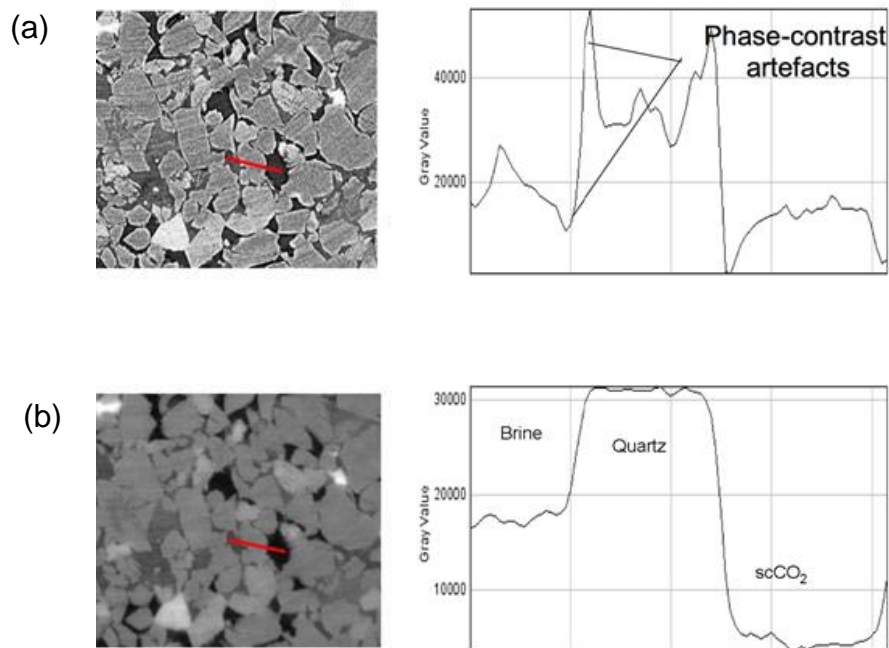


Figure 32: Reconstruction CT Images Using Paganin's Single Distance Algorithm. (a) Conventional Reconstructed CT Images Have Sharp Gray Value Jumps at Boundaries of Different Phases. (b) By Using the Paganin's Single Distance Algorithm to Reconstruct CT Images, the Phase-Contrast Artefacts Can Be Removed.

The peripheral pressure-temperature systems for the beryllium core holder were setup. The low-temperature high-pressure fluid circulation system was tested. Heat shrink tubing was used to wrap the Be vessel, serving as both a temperature insulation layer and an air barrier to prevent

moisture condensation outside of the Be vessel. The image below shows the high-pressure Be vessel connected with flexible PEEK tubing sitting on the micro-CT station (Figure 33).



Figure 33: High-Pressure Beryllium Chamber on the Micro-CT Station.

Subtask 5.2 Grain Scale Constitutive Modeling for Hydrate-Bearing Sediments

The fluid flow through a porous media, to a large extent, depends on precise relationships between permeability and porosity $k-\phi$. This relationship is inversely proportional to the square of flow tortuosity τ^2 . So, if the porosity-tortuosity $\phi - \tau$ relationship can be established, the fluid permeability in porous medium can be obtained by simply relying on the information of porosity. Therefore, the $\phi - \tau$ relationship in hydrate-bearing sediments was investigated using 2D pore network modeling.

Figure 34 (a) illustrates the tortuous flow through a 2D pore network, in which the red tubes represent the tubes with fluid flow and the tube thickness is proportional to the magnitude of the flow flux. The blue tubes represent the percolation path that carries the maximum amount of fluxes, which is the so-called critical path. The number of these blue tubes reflects the flow tortuosity across the tube network. Results in Figure 34(b) show that the tortuosity dependence on hydrate saturation is not monotonic. For each hydrate distribution pattern, tortuosity oscillates, with each decrease in tortuosity corresponding to a shift to another critical flow path. However, as a general trend, flow tortuosity increases with increasing hydrate saturation (i.e., with decreasing porosity), as observed in marine mud ([6] Iversen and Jørgensen, 1993) and porous matrix made of randomly placed rectangles ([7] Koponen et al., 1996).

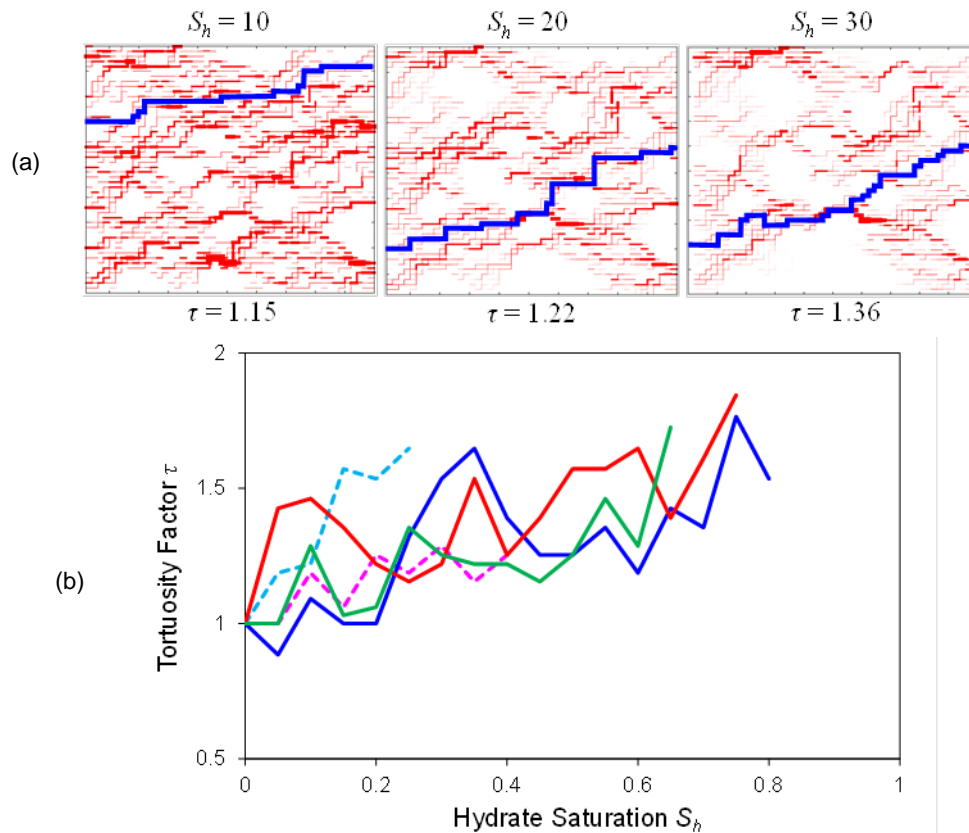


Figure 34: Hydrate Effect on Fluid Flow Tortuosity in Hydrate-Bearing Sediments. (a) Fluid Fluxed (Red Tubes) and the Critical Flow Path (Blue Tubes) across the Pore Network. (b) The Fluid Flow Tortuosity Oscillates with Hydrate Saturation, but the Generation Trend of the Tortuosity Increases with Hydrate Saturation.

To advance the grain-scale modeling of flow based on 3D CT images, fine quartzitic sands (F110) have been scanned using microfocus X-ray CT. The corresponding pore structure was extracted from these CT images using the rolling-ball algorithm. The F110 was selected because experimental data of their fundamental physical and hydrological properties, such as grain size distribution and permeability, are available. These data can be later used to validate our numerical simulation results.

Figure 35(a) shows the 3D micro-CT images of a 2cm×2cm×2cm F110 sample, with pixel resolution of 4.22micron. The extracted pore network from this scanning is shown in Figure 35(b).

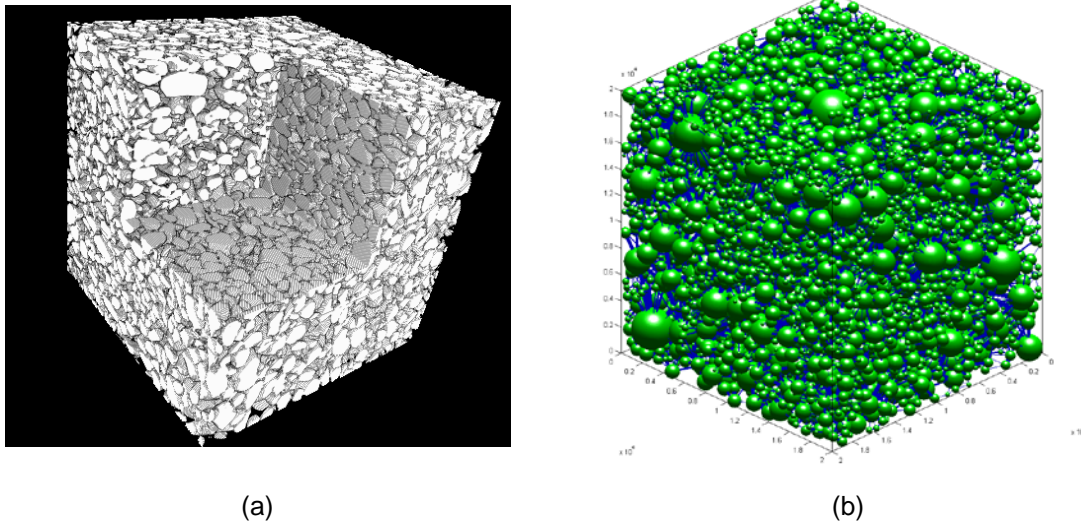


Figure 35: Pore Structure Extraction from CT Images. (a) 3D Micro-CT Images of F110 Sands. (b) Extracted Pore Network Structure from the CT Image. The Green Bubbles Represent the Pores and Their Volume is Scaled to the Bubble Size. The Blue Lines Represent the Throat Connecting Neighboring Pores and the Line Thickness Reflects the Pore Throat Size.

The CT images provide direct information about the physical properties of the scanned sample, such as mean grain size ($\mu_{d_grain} = 118\mu\text{m}$), grain size distribution, and specific surface. The extracted pore network provides information about the pore character, such as mean pore radius ($\mu_{r_pore} = 36.1\mu\text{m}$) and average pore connectivity ($cn = 7.95$). Figure 36 shows the relationship between pore connectivity and pore volume (or radius). Results suggest that the pore connectivity increases with the pore size, i.e., larger pores are directly connected to more neighboring pores.

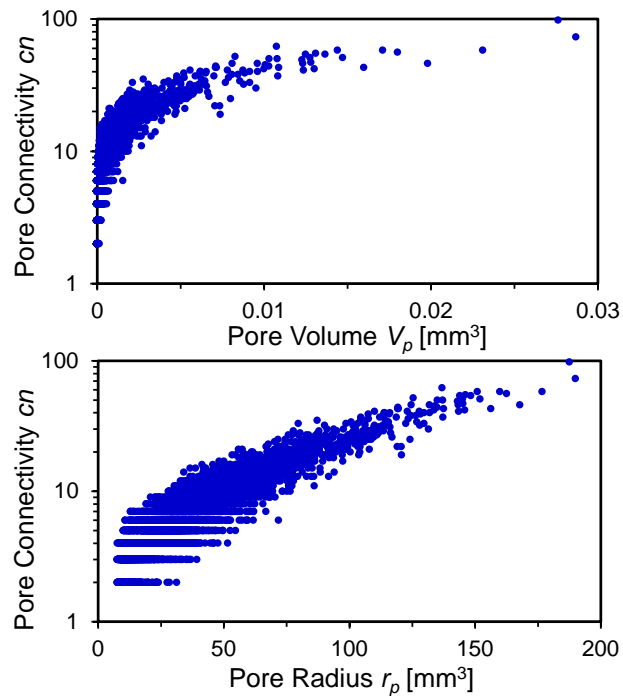


Figure 36: In Unconsolidated Sandy Specimen, the Pore Connectivity (cn) Increases with Pore Volume or Pore Radius.

References:

- [5] Weitkamp, T., Haas, D., Wegryzynek, D., and Rack, A., "ANKAphase: Software for Single-Distance Phase Retrieval from Inline X-Ray Phase-Contrast Radiographs," *Journal of Synchrotron Radiation*, 18(4), 617-629, 2011.
- [6] Iversen, N., and Jørgensen, B.B., "Diffusion Coefficients of Sulfate and Methane in Marine Sediments: Influence of Porosity," *Geochimica et Cosmochimica Acta*, 57(3), 571-578, 1993.
- [7] Koponen, A., Kataja, M., and Timonen, J., "Tortuous Flow in Porous Media," *Physical Review E*, 54(1), 406, 1996.

Changes in Approach:

Nothing to report during this activity period.

Problems or Delays:

Nothing to report during this activity period.

Changes in Key Personnel and Partnerships:

Nothing to report during this activity period.

Technology Transfer Activities or Product Produced:

A manuscript on 2D pore network study of fluid flow in hydrate-bearing sediments has been published on *Geophysical Research Letters*:

Dai, S., and Seol, Y., "Water Permeability in Hydrate-Bearing Sediments: A Pore-Scale Study," published *Geophysical Research Letters*, 41(12): p. 4176-4184, 2014.

4.0 Risk Analysis

Potential risks were identified as per the Project Risk Register in the PMP. All other risks noted in the register remained in force as originally identified. No new risks to project success were identified.

5.0 Milestone Status

The status of each major milestone is shown below in Table 4. Planned and actual milestone due dates have been revised to match the active Project Management Plan (PMP).

Table 4: Natural Gas Hydrate Research Support Milestone Status

Milestone Identifier	Title	Planned Date	Actual/ Forecast Completion	Milestone Status	Activities Driving Milestone	Activity Percent Complete	Comments/ Variance Analysis
Task 2.0 Reservoir Simulation of Gas Hydrates Production Field Tests							
M1.14.2.A	Development and distribution of elementary problem sets for code comparison study.	12/31/13	03/31/14	Completed		100%	None
M1.14.2.B	Development and distribution of Ignik Sikumi-based problem sets for code comparison study.	04/30/14	04/30/14	Completed		100%	None
M1.14.2.C	Complete simulations of production and flow modeling representative of a long-term depressurization test and modeling-based assessment of the potential for methane production from CO ₂ /N ₂ exchange test.	06/30/14	09/30/14	Delayed		75%	Site selection and new dataset delayed the progress.
Task 3.0 Developing Constitutive Models of Various Hydrate-Bearing Sands							
M1.14.3.A	Complete tri-axial geomechanical strength and deformability tests on CH ₄ and CO ₂ -hydrate-bearing sediments.	03/31/14	08/31/14	Delayed		40%	CO ₂ hydrate mechanical test.
M1.14.3.B	Complete data analysis for tri-axial tests and development of a constitutive model defining the relationship between hydrate saturation and elastoplastic soil behavior parameters.	09/30/14	09/30/14	In progress		60%	None
Task 4.0 Assessment of Gas Exchange Processes of CH₄ Hydrate with CO₂ under Reservoir Conditions							
M1.14.4.A	Complete CO ₂ (and/or CO ₂ /N ₂ mixture) - CH ₄ gas exchange mechanism tests with Raman spectroscopy.	03/31/14	08/31/14	Delayed		60%	New Raman laser source and detector installed and new tests resumed.

Milestone Identifier	Title	Planned Date	Actual/Forecast Completion	Milestone Status	Activities Driving Milestone	Activity Percent Complete	Comments/Variance Analysis
M1.14.4.B	Complete the measurements of CO ₂ (and/or CO ₂ /N ₂ mixture) - CH ₄ exchange kinetics with the presence of free water.	03/31/14	06/30/14	Completed		100%	None
M1.14.4.C	Complete comparative analysis for gas exchange kinetics data from experiments conducted at: NETL, LBNL, and PNNL (if available).	06/30/14	06/30/14	Completed		100%	No data available from LBNL or PNNL
5.0 Pore Scale Visualization and Characterization of Hydrate-Bearing Sediments							
M1.14.5.A	Complete development of pore scale imaging procedures and collection of hydrate images of hydrate-bearing sediments.	03/31/14	03/31/14	Completed		100%	None
M1.14.5.B	Complete development of grain scale constitutive models for hydrate-bearing sediments based on CT images.	09/30/14	09/30/14	In progress		50%	None
Milestone Status Key:							
Blue = Complete							
Green = Forecast Date is equal to or less than the planned completion							
Yellow = Forecast Date is greater than the planned completion by 1 to 30 days							
Red = Forecast Date is greater than the planned completion date by more than 30 days							

6.0 Schedule Status

Data comparison for Subtask 4.3 has been cancelled due to unavailability of other kinetic data from LBNL or PNNL. Also, column tests for gas production using gas exchange (Subtask 4.2) have been cancelled due to low efficiency of gas recovery.

The SARS permit for using beryllium core holder with the micro CT scanner was granted and shakedown activities for experiments (Subtask 5.2) are in progress.

7.0 Budget and Cost Status

The budget (plan) for FY14-Q3 was \$157K while the actual cost was \$260K, resulting in a negative cost variance of \$103K. Cumulative to date, the budget (plan) was \$426K while the actual cost was \$409K, resulting in a cost variance of \$17K.

Figure 37 below and Table 5 and Table 6 in Appendix A show detailed cost information for FY14.



Figure 37: Natural Gas Hydrate Research Cost Performance Histogram (\$ x 1,000).

8.0 References

References are listed in Section 3.0 of this report.

Appendix A: Budget and Cost Status

Table 5: Natural Gas Hydrate Research Field Work Proposal Budget Status (Current Period)

DOLLARS IN THOUSANDS													
CURRENT PERIOD													
Title	WBS	PLAN FY14 - Q1	ACTUAL FY14 - Q1	VAR FY14 - Q1	PLAN FY14 - Q2	ACTUAL FY14 - Q2	VAR FY14 - Q2	PLAN FY14 - Q3	ACTUAL FY14 - Q3	VAR FY14 - Q3	PLAN FY14 - Q4	ACTUAL FY14 - Q4	VAR FY14 - Q4
Project Management and Outreach	1	\$2	\$3	(\$1)	\$2	\$3	(\$1)	\$2	\$2	(\$1)	\$2		
Reservoir Simulation of Gas Hydrates Production Field Tests	2	\$18	\$0	\$18	\$20	\$14	\$6	\$30	\$11	\$19	\$96		
Developing Constitutive Models of Various Hydrate-Bearing Sands	3	\$27	\$0	\$27	\$27	\$36	(\$9)	\$51	\$109	(\$58)	\$27		
Assessment of Gas Exchange Processes of CH4 Hydrate with CO2 under Reservoir Conditions	4	\$21	\$16	\$5	\$54	\$24	\$31	\$23	\$111	(\$87)	\$21		
Pore Scale Visualization and Characterization of Hydrate-Bearing Sediments	5	\$23	\$0	\$23	\$23	\$0	\$23	\$23	\$0	\$23	\$23		
ORD OH		\$24	\$24	\$0	\$24	\$24	\$0	\$24	\$24	\$0	\$24		
Fee		\$2	\$0	\$2	\$2	\$5	(\$2)	\$5	\$2	\$2	\$7		
Total		\$117	\$43	\$73	\$153	\$106	\$46	\$157	\$260	(\$103)	\$199		

Includes costs for general infrastructure support.

Table 6: Natural Gas Hydrate Research Field Work Proposal Budget Status (Cumulative)

DOLLARS IN THOUSANDS													
CUMULATIVE													
Title	WBS	PLAN FY14 - Q1	ACTUAL FY14 - Q1	VAR FY14 - Q1	PLAN FY14 - Q2	ACTUAL FY14 - Q2	VAR FY14 - Q2	PLAN FY14 - Q3	ACTUAL FY14 - Q3	VAR FY14 - Q3	PLAN FY14 - Q4	ACTUAL FY14 - Q4	VAR FY14 - Q4
Project Management and Outreach	1	\$2	\$3	(\$1)	\$4	\$6	(\$2)	\$6	\$8	(\$3)	\$8		
Reservoir Simulation of Gas Hydrates Production Field Tests	2	\$18	\$0	\$18	\$38	\$14	\$24	\$67	\$25	\$42	\$163		
Developing Constitutive Models of Various Hydrate-Bearing Sands	3	\$27	\$0	\$27	\$53	\$36	\$17	\$104	\$144	(\$41)	\$130		
Assessment of Gas Exchange Processes of CH4 Hydrate with CO2 under Reservoir Conditions	4	\$21	\$16	\$5	\$75	\$40	\$35	\$99	\$151	(\$52)	\$119		
Pore Scale Visualization and Characterization of Hydrate-Bearing Sediments	5	\$23	\$0	\$23	\$45	\$0	\$45	\$68	\$0	\$68	\$91		
ORD OH		\$24	\$24	\$0	\$49	\$49	\$0	\$73	\$73	\$0	\$98		
Fee		\$2	\$0	\$2	\$5	\$5	(\$0)	\$9	\$7	\$2	\$16		
Total		\$117	\$43	\$73	\$269	\$150	\$119	\$426	\$409	\$17	\$625		

Includes costs for general infrastructure support.